Flow prediction in brain aneurysms using OpenFOAM

M. de Groot

September 2, 2014

Abstract

Methods to detect aneurysms in the brain have existed for some decades. A relatively new method, 3D rotational angiography (3DRA), has received a lot of attention in the last decade, because with it additional smaller aneurysms can be detected more easily in comparison to more conventional methods. The voxel data of 3DRA allows for reconstruction of the blood vessel geometry with relative ease, which makes it of particular interest in the study of computational fluid dynamics (CFD). Predictions made based on a CFD analysis are believed to become more and more important and may have consequences for the type of treatment a particular patient receives.

The immersed boundary (IB) method is one of many CFD methods available to perform numerical simulations. The strength of the IB method is that no complex or time consuming grid generation is required. Instead, it uses a Cartesian grid in which the geometry is immersed, and is only concerned with determining whether a grid cell is part of the geometry or not. Its simplicity makes the IB method an excellent combination with 3DRA. A disadvantage of the IB method is that often only a small portion of the grid cells is part of the geometry, especially for complex geometries, making it a rather expensive method in terms of computation time. In this thesis an effort is made to utilise the simplicity of the IB method to perform numerical simulations of blood flow in the human brain without having to rely on grid cells which are not part of the geometry. Simulations are performed with an open source CFD software package, called OpenFOAM, which requires a number of input files to specify the grid. The challenge is to find an efficient way to remove the cells which are not part of the geometry from the grid and to generate the input files accordingly.

This is succesfully done and different steps which have to be taken to ensure that the input files are according to the OpenFOAM format are presented in this thesis. The previously mentioned approach is validated by studying flow through simple model geometries and subsequently a realistic geometry, reconstructed from 3DRA data. Comparable results are found to a study adopting the IB method. Potential differences are pointed out and discussed.

Contents

Chapter 1

Introduction

A description is given of how the equations which govern fluid flow are solved using the open source CFD software package OpenFOAM and how these computations can be done in parallel. First, the governing equations for fluid flow, the Navier-Stokes equations, are presented. Subsequently, an explanation of the adopted numerical method in OpenFOAM is given. Finally, it is shown how parallel computation can be done in OpenFOAM.

Starting from a masking function, the key element in a volume-penalising immersed boundary method which represents the geometry by taking either values '0' or '1' depending on whether a cell is in the fluid part or in the solid part of the domain, a geometry is constructed in OpenFOAM which only consists of cells which are in the fluid part of the domain. The method is validated with Poiseuille flow through a cylindrical pipe. Several measures are defined which are used to check how sensitive the solution is to refinement of the grid. Finally, the computational domain of the cylindrical pipe is decomposed in different ways, which is then used to see how the speedup of the computation is affected by different decompositions.

Another convergence study is done for Poiseuille flow through curved pipes, which have a sinusoidal shape. For these type of flows no analytical solution exists. Therefore, the previously mentioned measures are slightly altered such that they can still be used to investigate how sensitive the solution is to grid refinement. Finally, a realistic geometry is taken under consideration. A comparison is done between Poiseuille flow and physiologically relevant flow. Significant differences in flow behavior are observed and an attempt is made to test the sensitivity of the solution to refinement of the grid.

The thesis is organised as follows. In Chapter 2 the adopted numerical method in OpenFOAM is described, followed by an explanation of parallel computation in OpenFOAM. The construction of geometries from the masking function of a volume-penalising immersed boundary method is explained in Chapter 3, after which it is validated with Poiseuille flow through a cylindrical pipe. The speedup of computation is tested by decomposing the cylindrical pipe in several ways. In Chapter 4 also Poiseuille flow through curved pipes is considered, which then bridges the gap to Poiseuille flow through realistic geometries. The chapter is concluded with physiologically relevant flow through through a realistic geometry.

Chapter 2

Computational model

This chapter is devoted to the Navier-Stokes equations and their respresentation in OpenFOAM. The process of solving these equations in OpenFOAM is explained in detail through an example of an initial-boundary value problem for the diffusion equation.

2.1 Navier-Stokes equations

The motion of incompressible Newtonian fluids in Cartesian coordinates is governed by the continuity equation

$$\nabla \cdot \mathbf{u} = 0, \tag{2.1}$$

which reflects the conservation of mass, and the equations describing conservation of momentum, which are known as the Navier-Stokes equations,

$$\partial_t \mathbf{u} + \nabla \cdot (\mathbf{u}\mathbf{u}^T) = -\nabla P + \nabla \cdot (\nu \nabla \mathbf{u}), \tag{2.2}$$

with fluid velocity $\mathbf{u}(\mathbf{x}, t)$, kinematic pressure $P(\mathbf{x}, t)$ and kinematic viscosity ν.

Boundary conditions are $\mathbf{u} = \mathbf{0}$ at solid boundaries and the domain is periodic in the x-direction. Because pressure is relative in a closed incompressible system, the absolute value of pressure is not important. Hence, the initial conditions for velocity are chosen as $\mathbf{u} = \mathbf{0}$ and for pressure as $P = 0$.

The volumetric flow rate Q is fixed and a pressure drop is imposed to force the flow. To be able to impose periodic boundary conditions on the pressure and to have a pressure drop, the pressure term has to be modified. This can be achieved by splitting the pressure gradient in a gradient of the periodic component of the pressure and a term which gives the desired pressure drop as follows

$$\nabla P(\mathbf{x}, t) = \nabla \tilde{p}(\mathbf{x}, t) + \nabla p(t). \tag{2.3}$$

2.2 Numerical method and OpenFOAM

Consider the diffusion equation

$$\partial_t T - \nabla \cdot (D_T \nabla T) = 0, \tag{2.4}$$

with temperature $T = T(\mathbf{x}, t)$ and diffusion coefficient D_T. This equation is represented in OpenFOAM as

```
solve
(
    fvm::ddt(T) - fvm::laplacian(DT, T)
);
```

which is very intuitive; it looks similar to (2.4). Terms starting with `fvm::` are implicit terms and explicit terms start with `fvc::`.

Now consider the following one-dimensional initial-boundary value problem for the diffusion equation

$$\begin{cases} \partial_t T - \partial_x (D_T \partial_x T) = 0 & \text{for } 0 < x < L_x \text{ and } t > 0, \\ T(x,0) = f(x), & \text{for } 0 < x < L_x, \\ T(0,t) = T(L_x,t) = 0, & \text{for } t > 0, \end{cases} \tag{2.5}$$

with constant diffusion coefficient D_T.

By introducing the scaling

$$\hat{x} = \frac{x}{X}, \quad \hat{t} = \frac{t}{\tau}, \quad \hat{T} = \frac{T}{\mathcal{T}}, \quad \hat{f} = \frac{f}{\mathcal{T}}, \tag{2.6}$$

the problem can be transformed to the dimensionless initial-boundary value problem

$$\begin{cases} \partial_t T - \partial_x (1\, \partial_x T) = 0 & \text{for } 0 < x < 1 \text{ and } t > 0, \\ T(x,0) = f(x), & \text{for } 0 < x < 1, \\ T(0,t) = T(1,t) = 0, & \text{for } t > 0, \end{cases} \tag{2.7}$$

where hats have been dropped.

In the following an example case in OpenFOAM will be worked out. The problem given above will be represented as a rectangular copper rod with 1 meter length with initial temperature distribution $f(x) = T_0 = 100$. OpenFOAM uses physical quantities to be able to perform dimension checks in its calculations. An analytical solution from the dimensionless problem will be used later, after rescaling, to validate the numerical solution which is obtained with OpenFOAM.

Setting up a case consists of several steps:

- Construct the mesh in the OpenFOAM mesh format, polyMesh
- Set parameters related to the problem
- Define initial and boundary conditions for each of the variables
- Select numerical schemes for each of the terms in the differential equation
- Specify solving algorithm and stop criteria per variable
- Set time control parameters and output settings

For a simple case like this, the geometry can easily be constructed using the mesh generation utility blockMesh, which is supplied with OpenFOAM. Geometries in OpenFOAM are always three-dimensional, even for a one-dimensional problem like in this example. In a dictionary file called blockMeshDict, which is located in the 'constant/polyMesh' directory for a given case, settings denoted by keywords are specified which are used by blockMesh to generate mesh files according to the polyMesh format. Below is the relevant part of the blockMeshDict file for this case. The scale of the problem is defined with the keyword `convertToMeters`, which is 1 meter in this case. With the keyword `vertices` the (unscaled) coordinates of the corners of the rod are defined. The position of each coordinate in the list determines its label $(0, 1, \ldots)$. On the line labeled with the keyword `blocks` three characteristics of the mesh are defined. First the geometry is defined by giving the coordinate labels in a specific order, followed by the number of cells in each direction and finally the expansion ratios of the cells in each direction. These expansion ratios are defined as the ratio between the width of the last cell to the width of the first cell. The boundaries are specified in the last part denoted by the keyword `boundary`.

```
convertToMeters 1;

vertices
(
    (0 0 0)
    (1 0 0)
    (1 0.1 0)
    (0 0.1 0)
    (0 0 0.1)
    (1 0 0.1)
    (1 0.1 0.1)
    (0 0.1 0.1)
);

blocks
(
    hex (0 1 2 3 4 5 6 7) (1000 1 1) simpleGrading (1 1 1)
);

boundary
(
    patch1
    {
        type patch;
        faces
        (
            (0 4 7 3)
        );
    }
    patch2
    {
        type patch;
        faces
        (
            (1 2 6 5)
        );
    }
    patch3
    {
        type empty;
        faces
        (
            (0 3 2 1)
            (4 5 6 7)
            (0 1 5 4)
            (2 3 7 6)
        );
    }
);
```

The keywords `patch1` and `patch2` correspond to the boundaries at $x = 0$ and $x = 1$ respectively and the part denoted by the keyword `patch3` labels the remaining sides of the rod as `empty`, which causes OpenFOAM to interpret the problem as a one-dimensional problem. After running blockMesh a number of files will be generated in the 'constant/polyMesh' directory. The file *points* containing coordinates of vertices of the cells, the file *faces* defining faces of the cells, the files *owner* and *neighbour* defining connectivity of the mesh and the file *boundary* giving information about boundaries of the mesh.

The only parameter in this problem is the diffusion coefficient, which for copper is $D_T = 1.11 \cdot 10^{-4}$, and it is specified in the dictionary file transportProperties, which can be found in the 'constant' directory, as follows

```
DT              DT [ 0 2 -1 0 0 0 0 ] 1.11e-04;
```

The seven scalars delimited by square brackets correspond to the powers of the SI base units, which are defining the units of measurement (m^2/s) for the specified quantity.

Initial and boundary conditions are specified in the file T in the '0' directory. For this example the file is shown below. First, the dimensions of the variable T (K) are defined. Of course, for this particular example one would rather think in degrees Celcius (°C), but a transformation from degrees Celcius to Kelvin does not change the nature of the problem. On the next line, denoted by `internalField`, the initial value (100) is assigned to all cells. More specificly, the values are defined at the centres of the cells. The last part, with the keyword `boundaryField`, specifies boundary conditions; $T = 0$ at $x = 0$ and $x = 1$, and an `empty` boundary on the remaining sides of the rod, as before.

```
dimensions      [0 0 0 1 0 0 0];

internalField   uniform 100;

boundaryField
{
    patch1
    {
        type            fixedValue;
        value           uniform 0;
    }

    patch2
    {
        type            fixedValue;
        value           uniform 0;
    }

    patch3
    {
        type            empty;
    }
}
```

Integration of (2.4) over a control volume V with boundary S gives

$$\partial_t \int_V T \, dV - \int_S (D_T \nabla T) \cdot \mathbf{dS} = 0. \tag{2.8}$$

If T_i is defined as

$$T_i^n := T_i(t = t_n) = \frac{1}{V_i} \int_{V_i} T(\mathbf{x}, t = t_n) \, dV, \tag{2.9}$$

then (2.8) becomes

$$(\partial_t T_i)^{n+1} - \frac{1}{V_i} \sum_{f_i} (D_T \nabla T)_{f_i}^{n+1} \cdot \mathbf{S}_{f_i} = 0. \tag{2.10}$$

The numerical schemes used for the discretisation in (2.10) can be found in the dictionary file *fvSchemes*, which is located in the 'system' directory. Several entries which are typically found in the *fvSchemes* file are shown below. The time derivative is discretised using a backward Euler method. The value of $(\nabla T)_{f_i}$ is computed by using the values of T_i in the adjoining cells, thus assuming a linear change over the face.

```
ddtSchemes
{
    default         Euler;
}

gradSchemes
{
    default         none;
    grad(T)         Gauss linear;
}

divSchemes
{
    default         none;
}

laplacianSchemes
{
    default         none;
    laplacian(DT,T) Gauss linear corrected;
}

interpolationSchemes
{
    default         none;
}

snGradSchemes
{
    default         none;
}

fluxRequired
{
    default         no;
}
```

Hence, the worked out discretisation looks like

$$\frac{T_i^{n+1} - T_i^n}{\Delta t}\Delta x_i - D_T \frac{T_{i-1}^{n+1} - 2T_i^{n+1} + T_{i+1}^{n+1}}{\Delta x_i} = 0. \tag{2.11}$$

The solving algorithm is specified in the dictionary file fvSolution, which can be found in the 'system' directory. For this case a conjugate gradient method (`PCG`) is used, which is preconditioned with an incomplete Cholesky factorization (`DIC`), as can be seen below. The algorithm stops once the error between the left- and right-hand side of Equation 2.10 is smaller than 10^{-6}.

```
solvers
{
    T
    {
        solver          PCG;
        preconditioner  DIC;
        tolerance       1e-06;
        relTol          0;
    }
}

SIMPLE
{
    nNonOrthogonalCorrectors 0;
}
```

The most relevant parts of the dictionary file controlDict located in the 'system' directory, in which time and output control are specified are shown below. The keywords are very intuitive. The simulated time is from $t = 0$ to $t = 900$ (s) with time steps $\Delta t = 1$. Every 60 seconds of simulated time the solution is written to a file in a directory named after the corresponding time $(60, 120, \dots)$, with six significant figures.

```
startFrom       startTime;

startTime       0;

stopAt          endTime;

endTime         900;

deltaT          1;

writeControl    runTime;

writeInterval   60;

writeFormat     ascii;

writePrecision  6;
```

An analytical solution to (2.7) is

$$T(x,t) \approx \frac{4T_0}{\pi}\sin(\pi x)e^{-\pi^2 t}, \quad \text{for } t \geq \frac{1}{\pi^2} \tag{2.12}$$

Figure 2.1 shows the numerical solution to (2.5) for the copper rod at several times and the analytical solution in (2.12) at $t = 9.99 \cdot 10^{-2}$, which is slightly less than $\frac{1}{\pi^2}$ and corresponds to $t = 900$ in physical quantities. The numerical solution clearly agrees very well to the analytical solution.

In OpenFOAM the Navier-Stokes equations can be solved using a method which splits the solution procedure for velocity and pressure, called the PISO (Pressure-Implicit with Splitting of Operators) method [1]. The PISO method consists of several steps, a predictor step and several corrector steps. The most relevant parts of the implementation of the Navier-Stokes equations and the PISO method are seen below.

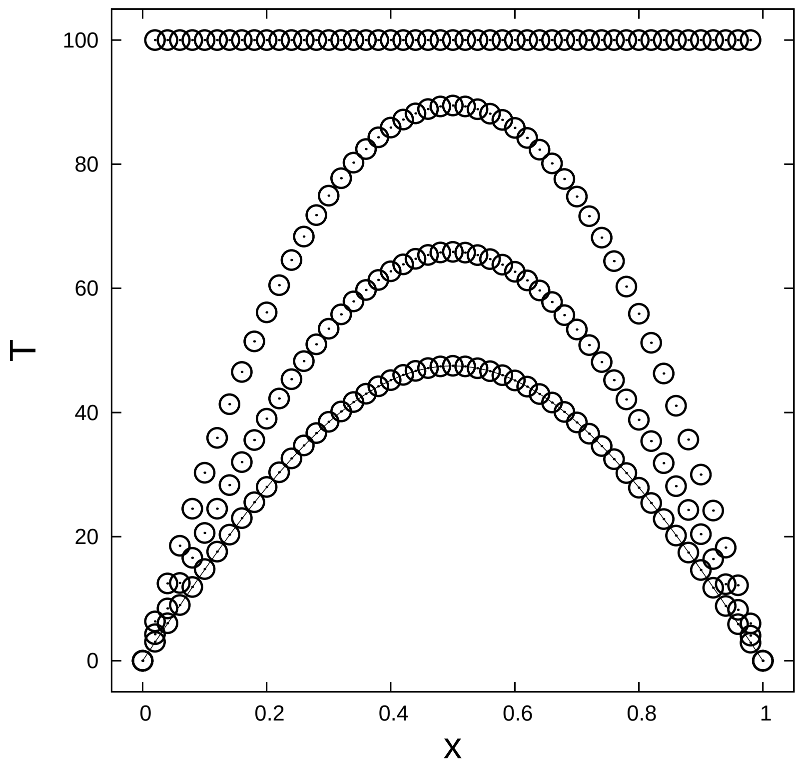

Figure 2.1: Numerical solution to the diffusion problem in a copper rod with an initial constant temperature at different times. Time ranges from $t = 0$ to $t = 900$ with increment $\Delta t = 300$. The solid curve corresponds to the analytical solution to (2.7) rescaled to physical quantities.

```
fvVectorMatrix UEqn
(
    fvm::ddt(U)
  + fvm::div(phi, U)
  + sgsModel->divDevBeff(U)
 ==
    flowDirection*gradP
);

if (momentumPredictor)
{
    solve(UEqn == -fvc::grad(p));
}

volScalarField rAU(1.0/UEqn.A());

for (int corr=0; corr<nCorr; corr++)
{
    U = rAU*UEqn.H();
    phi = (fvc::interpolate(U) & mesh.Sf())
        + fvc::ddtPhiCorr(rAU, U, phi);

    fvScalarMatrix pEqn
    (
        fvm::laplacian(rAU, p) == fvc::div(phi)
    );

    pEqn.setReference(pRefCell, pRefValue);

    if (corr == nCorr-1)
    {
        pEqn.solve(mesh.solver(p.name() + ''Final''));
    }
    else
    {
        pEqn.solve(mesh.solver(p.name()));
    }

    phi -= pEqn.flux();

    U -= rAU*fvc:grad(p);
    U.correctBoundaryConditions();
}
```

The Navier-Stokes equations can be easily recognised.

Integration of the Navier-Stokes equations over a control volume V with boundary S and simplifying the diffusion term, as was done in the implementation in OpenFOAM, gives after applying the divergence theorem,

$$\partial_t \int_V \mathbf{u}\, dV + \int_S (\mathbf{u}\mathbf{u}^T)\, d\mathbf{S} = -\int_S \tilde{p}\, d\mathbf{S} - \nabla p \int_V dV + \int_S (\nu \nabla \mathbf{u})\, d\mathbf{S}. \tag{2.13}$$

If $\mathbf{U}_i$ and p_i are defined as

$$\mathbf{U}_i^n := \mathbf{U}_i(t = t_n) = \frac{1}{V_i} \int_{V_i} \mathbf{u}(\mathbf{x}, t = t_n)\, dV, \tag{2.14}$$

$$p_i^n := p_i(t = t_n) = \frac{1}{V_i} \int_{V_i} \tilde{p}(\mathbf{x}, t = t_n)\, dV. \tag{2.15}$$

then (2.13) becomes

$$\partial_t \mathbf{U}_i + \frac{1}{V_i}\sum_{f_i}(\mathbf{U}_{f_i}\mathbf{U}_{f_i}^T)\mathbf{S}_{f_i} = -\frac{1}{V_i}\sum_{f_i} p_{f_i}\mathbf{S}_{f_i} - \nabla p + \frac{1}{V_i}\sum_{f_i}(\nu(\nabla \mathbf{U})_{f_i})\mathbf{S}_{f_i} \tag{2.16}$$

on a Cartesian grid, where $\mathbf{S}_{f_i}$ is the outward pointing normal vector of face f_i of control volume V_i.

Chapter 3

Immersed boundary representation

In this chapter the problem of defining a flow problem suitable for simulation within OpenFOAM is looked into, starting from an alternative respresentation of the problem in terms of a masking function. In Section 3.1 these steps are specified for a cylindrical geometry and Section 3.2 is devoted to a computational analysis of Poiseuille flow.

3.1 From masking function to OpenFOAM

In this section the problem of creating a mesh from a masking function of a circle is considered. First, the requirements of OpenFOAM on the generated files is discussed. Second, the procedure is illustrated with an example.

Requirements of OpenFOAM on mesh

The OpenFOAM mesh format, polyMesh, supports arbitrary polyhedral cells with arbitrary polygonal faces, provided a set of conditions is satisfied [3].

- The position of each point is specified by three Cartesian coordinates, even when, for example, a two-dimensional problem is considered.
- The computational domain is completely covered by cells and cells do not overlap.
- Cells are convex and the cell centre is inside the cell.
- When all face area vectors of a cell point outwards, their sum should equal the zero vector up to machine precision. Additionally, edges of a cell are used by exactly two of its faces.
- Faces connect no more than two cells.
- For internal faces the face normal vector points into the cell with the larger label, and for boundary faces the face normal vector points outwards.

Masking function of a circle

In the volume-penalising immersed boundary method adopted by Mikhal [2] geometries are respresented by immersing it in a Cartesian grid. A forcing term in the Navier-Stokes equations, which can be either switched 'off' and 'on' depending on whether the grid cell is in the 'fluid' or 'solid' part of the domain, ensures that there is no flow outside the geometry. Consider an example of a masking function of a circle on a grid with five cells in both the horizontal and the vertical direction, as seen in Figure 3.1. If a cell is entirely within the circle, it is treated as part of the fluid domain. Otherwise, it is labeled as part of the solid domain. In the fluid domain the masking function attains the value 0 and in the solid domain the value 1. Because this is a fairly simple case, it is readily checked whether a cell is entirely within the geometry. For other cases later on in this thesis, the only condition on whether a cell is 'fluid' or 'solid' is whether the cell centre is inside the geometry.

By removing the cells that are part of the solid domain, the number of cells is reduced in this example by 80%. For more complex geometries, which are quite slender and possibly highly 3D contorted, the reduction in the number of cells can amount to 95%, which could result in a significant reduction of the amount of time needed to compute velocity and pressure fields, especially for large cases. The 'fluid' cells are labeled, starting from 0. The labeling as shown in Figure 3.2 is just one way to do it. In principle, other choices can be accepted as well. The labeling of the faces is restricted by one of the conditions mentioned above. Internal faces are labeled first and the labeling finishes with boundary faces. For each cell the faces are checked and the faces without label are given a label. If a cell has two or more faces without a label, the face which connects to the cell with the lower label is labeled first.

The face normal vectors are such that they point into the cell with the larger label for internal faces and outwards for boundary faces, as in Figure 3.3. The cell with the lower label is called the *owner* of the face and the cell with the larger label is called the *neighbour* of the face.

Figure 3.4 shows the masking function as the grid is refined twice, where the number of cells is doubled in each direction with each refinement. 'Solid' cells are shown in black and 'fluid' cells are shown in white. Clearly, with only two refinements, already a quite acceptable approximation to the circle is achieved, which obviously improves further with increasing resolution.

3.2 Poiseuille flow

In this section Poiseuille flow through a pipe is considered. First, the setting and several flow parameters are presented. Second, velocity profiles for different resolutions are compared to the analytical solution. Third, the observed convergence is quantified with several mathematical measures.

Setting and control parameters

Flow through a pipe with radius $R = 1$ (m) and length $L_x = 3$ (m) with volumetric flow rate $Q = \frac{\pi}{2}$ (m^3/s), thus with average streamwise velocity $\bar{u} = \frac{1}{2}$, and kinematic viscosity $\nu = \frac{1}{2}$ is considered. This flow corresponds to a Reynolds number $\mathrm{Re} = 1$.

The analytical solution to the Navier-Stokes equation for this flow is

$$u(x, y, z) = R(1 - y^2 - z^2), \quad v(x, y, z) = w(x, y, z) = 0. \tag{3.1}$$

In order to simulate the flow the immersed boundary method is used as a starting point and the pipe is considered to be immersed in a box of dimensions $3 \times 3 \times 3$ (m), and a uniform grid is applied to it with resolution $4 \times 2^k \times 2^k$ with $k = 3 \ldots 7$. In Figure 3.5 profiles, both numerical and

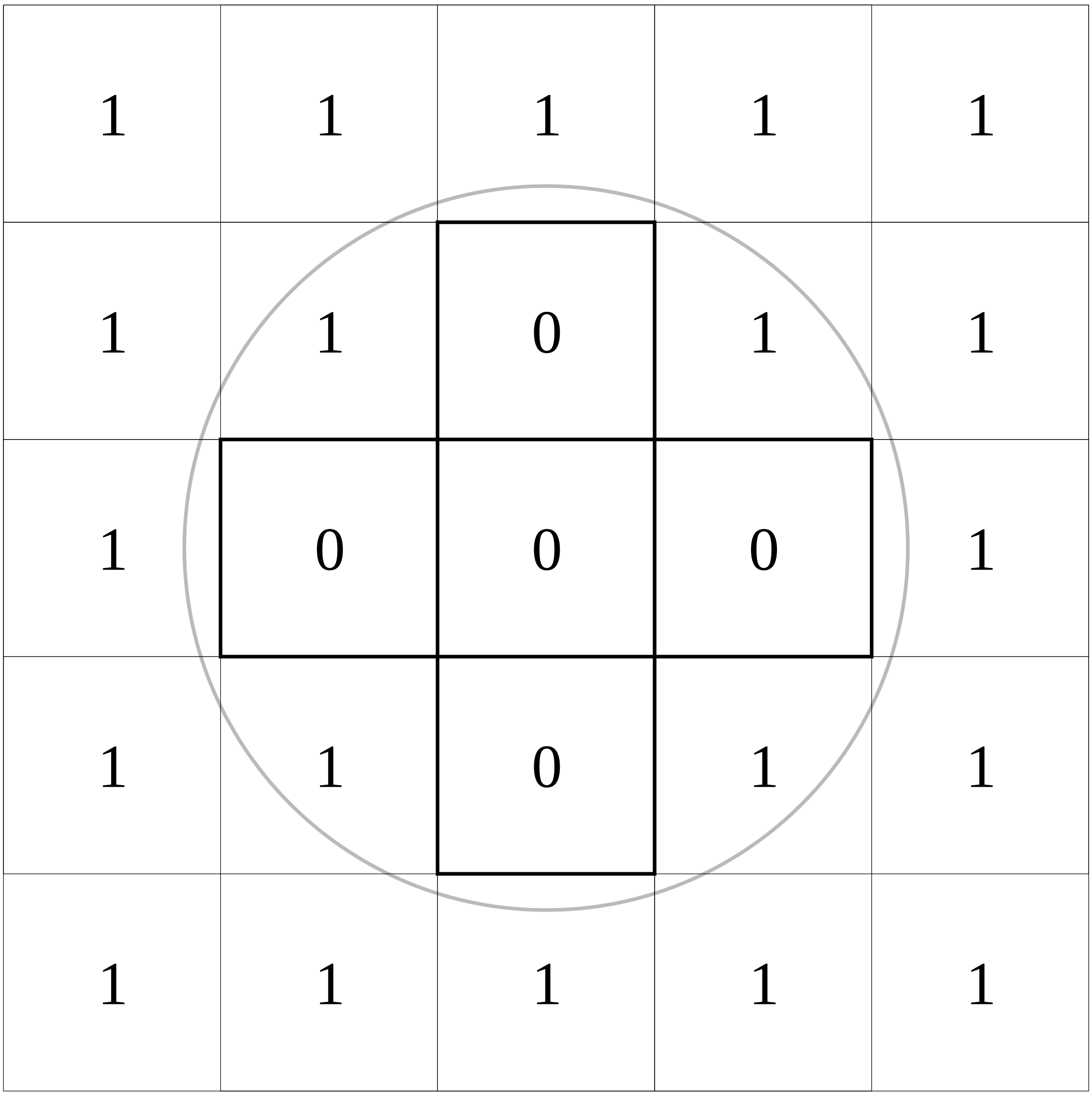

Figure 3.1: Illustration of a masking function for a cross section of a pipe. Cells which are entirely within the circle are part of the fluid domain and the masking function has value 0 there. For the remaining cells, which are part of the solid domain, the masking function has value 1.

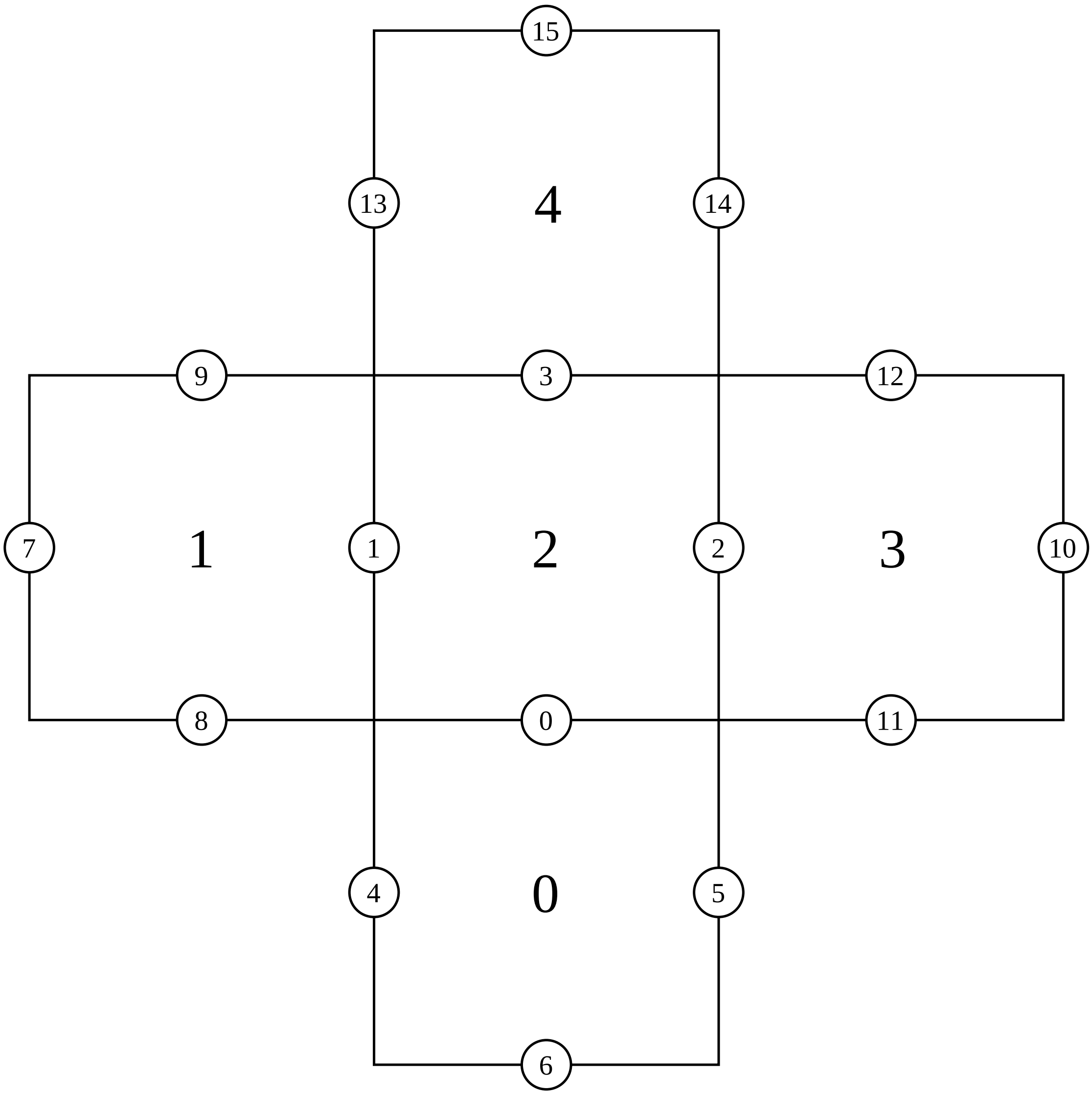

Figure 3.2: Illustration of the labeling of cells and faces. The labeling of cells is arbitrary, but the labeling of faces has to satisfy certain conditions.

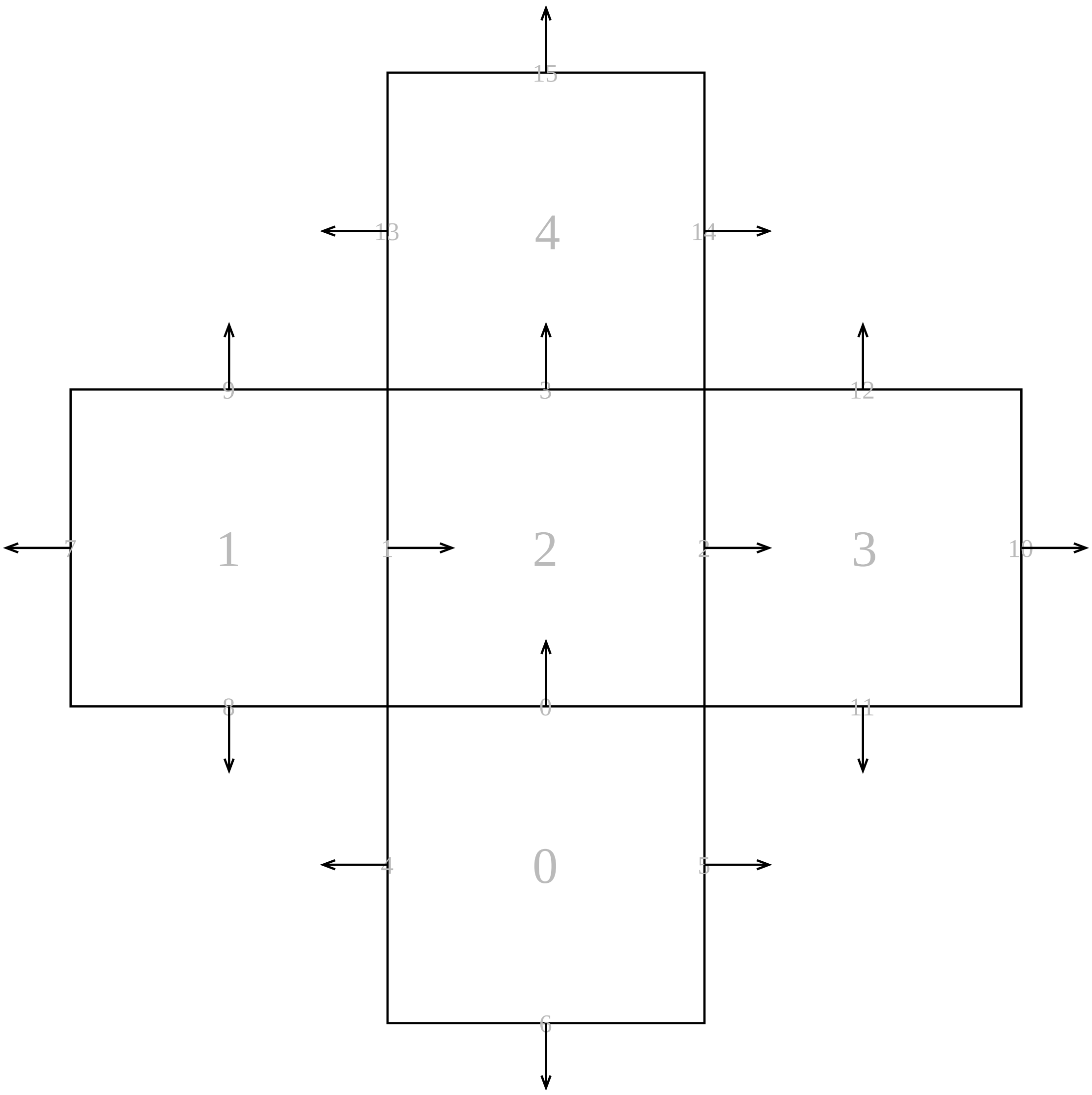

Figure 3.3: Illustration of the direction of the face normal vectors. Normal vectors of internal faces point into the cell with the larger label. Normal vectors of boundary faces points outwards.

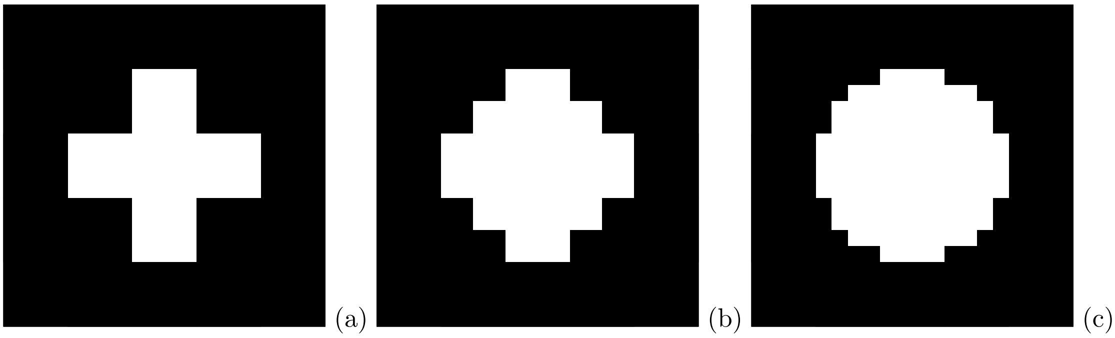

Figure 3.4: Illustration of the masking function as the grid is refined.

analytical, of the streamwise velocity u are shown. For $k \geq 5$ the numerical solution is already visually close to the analytical solution and the approximation gets better as k is increased. In order to quantify the apparent convergence different ways to measure the distance between the numerical and analytical solution are introduced.

To check convergence the distance between the numerical solutions and the analytical solution is measured with two different norms, i.e. the l^2-norm

$$||u_{N_z} - u||_2 = \sqrt{\sum_{n=1}^{N_z} (u_{N_z}(0,0,z_n) - u(0,0,z_n))^2}, \tag{3.2}$$

where z_n is a grid point, which depends on N_z, and the l^∞-norm

$$||u_{N_z} - u||_\infty = \max_{n=1 \dots N_z} |u_{N_z}(0,0,z_n) - u(0,0,z_n)|. \tag{3.3}$$

In Figure 3.6 these distances are compared as a function of N_z. Clearly, both distances converge with first order.

Being able to compare a numerical solution to an analytical solution is convenient but is often not possible for more complex geometries. For that reason, one might want to measure distances between a numerical solution and the analytical solution differently. Figure 3.7 shows how three different quantities converge to the exact value. Two lines, one showing the difference in the diameter of the pipe, measured as the difference between z_1 and z_{N_z}, and one showing the difference between the integrals over the streamwise velocity u from z_1 to z_{N_z}, where the integral over the numerical solution is found with a trapezoidal rule, marked with crosses and circles respectively, indicate first order convergence. The difference in the maximum streamwise velocity, which is shown as a line with triangle markers, appears to converge faster with second order.

Instead of measuring distances over a line one could compare quantities related to the entire volume of the pipe. Figure 3.8 shows the differences in the volume of the pipe (crosses), the volume integral over the streamwise velocity u (circles) and the volume integral over the kinetic energy $E = \frac{1}{2}(u^2 + v^2 + w^2)$ (triangles). The straight lines without markers have slope -1 and -2 respectively. Clearly, the three quantities converge with first order.

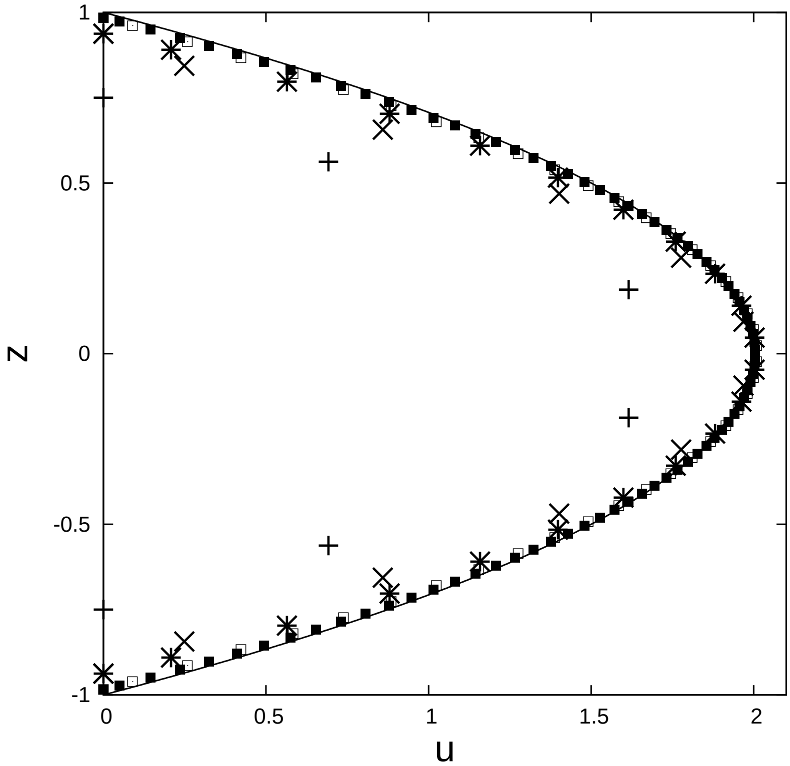

Figure 3.5: Velocity profiles for Poiseuille flow through a pipe of radius $R = 1$ for several resolutions. The number of grid points in the z-direction is $N_z = 2^k$, where $k = 3 \ldots 7$, marked with pluses, crosses, stars, open and filled squares respectively. The solid line corresponds to the analytical solution $u(x, 0, z) = R(1 - z^2)$.

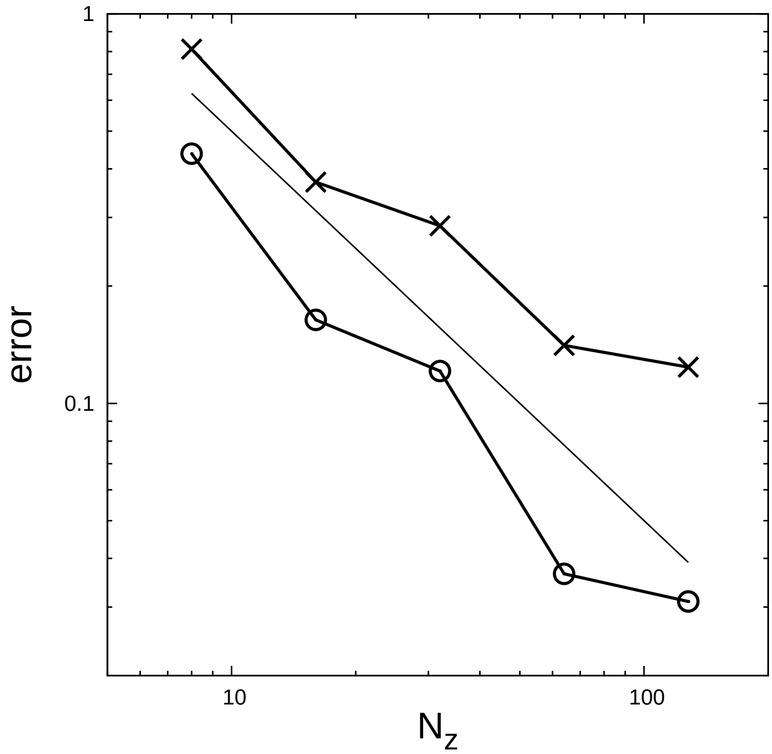

Figure 3.6: Convergence of the streamwise velocity for Poiseuille flow through a pipe of radius $R = 1$ towards the analytical solution $u(x, 0, z) = R(1 - z^2)$ in both the l^2-norm (crosses) and the l^∞-norm (circles). The straight line has slope -1.

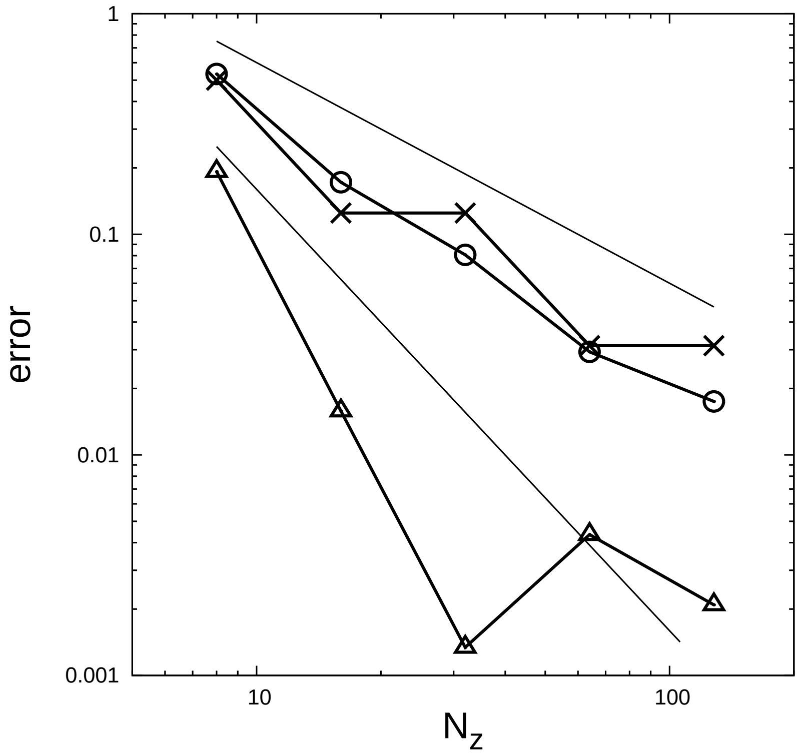

Figure 3.7: Convergence of several quantities with respect to the exact value for Poiseuille flow through a pipe of radius $R = 1$. The crosses correspond to the length of the line from bottom to top of the pipe in the z-direction, the circles to the integral of the streamwise velocity u over this line and triangles to the maximum streamwise velocity along this line. The straight lines have slope -1 and -2 respectively.

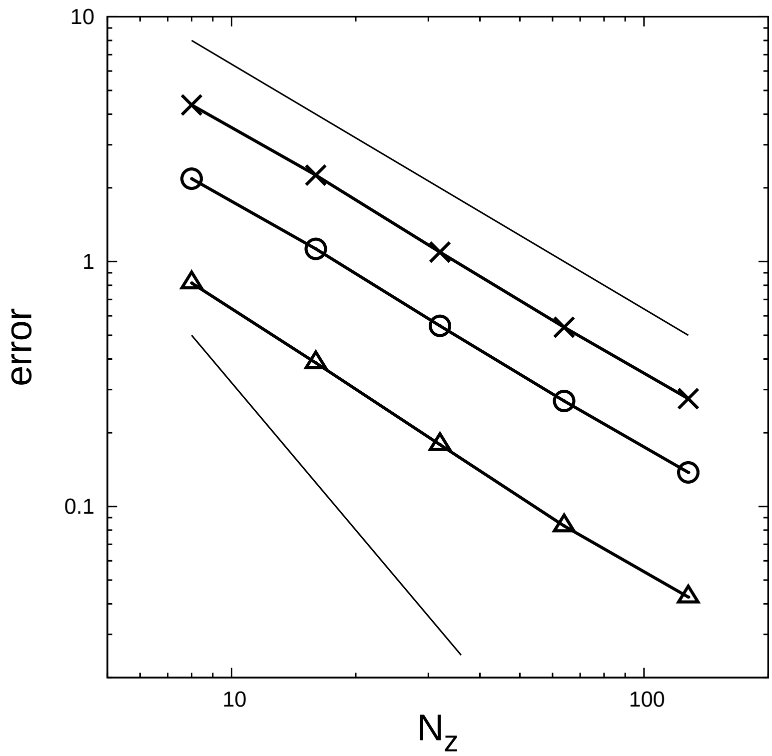

Figure 3.8: Convergence of several quantities with respect to the exact value for Poiseuille flow through a pipe of radius $R = 1$. The crosses correspond to the volume of the pipe, the circles to the streamwise velocity u integrated over the volume of the pipe and the triangles to the kinetic energy E integrated over the volume of the pipe, where $E = \frac{1}{2}(u^2 + v^2 + w^2)$. The straight lines without markers have slope -1 and -2 respectively.

Chapter 4

Applications

In this chapter flow through more realistic geometries is considered. First laminar flow through curved vessels is considered in Section 4.1 and this section is concluded with flow through a realistic geometry. In Section 4.2 flow with realistic flow parameters is examined and a comparison is made with laminar flow.

4.1 Curved and realistic vessels

In this section laminar flow through several curved vessels is considered and is concluded with laminar flow through a realistic geometry which is constructed from a masking function obtained after manipulation of a 3DRA scan.

The centerline of the curved vessels in this section is described by the curve $(x_c(s), y_c(s), z_c(s))$

$$x_c = 12s, \quad y_c = 2, \quad z_c = 4 + 2\epsilon \sin(2\pi(s - \frac{1}{4})) + 2(1-\epsilon)\sin(2\pi(s^3 - \frac{1}{4})), \tag{4.1}$$

with skewness-parameter $\epsilon \in [0, 1]$. The reference case with $\epsilon = 1$ is considered first. Two additional cases, with $\epsilon = 0.5$ and $\epsilon = 0.25$ respectively, are considered to try to explain unexpected behavior of the solution in the reference case.

Figure 4.1 shows slices of the velocity field through the center of the vessel for three different resolutions. At a coarse grid with resolution $32 \times 8 \times 16$ the solution respresents the flow rather poorly, but with one refinement to a resolution of $64 \times 16 \times 32$ the solution shows qualitatively agreement with the next refinement to a resolution of $128 \times 32 \times 64$.

In Figure 4.2 an illustration of the masking function on a plane through the center of the vessel is given together with profiles of the streamwise velocity at different streamwise locations at resolution $64 \times 16 \times 32$. These velocity profiles look similar to what was found in [2].

For different resolutions profiles of the streamwise velocity at several equidistant streamwise locations are shown in Figure 4.3. Note that grids with different resolution do not have coinciding grid points, because OpenFOAM uses a collocated grid, which results in slightly different streamwise locations as the resolution is increased. As the resolution is increased from $32 \times 8 \times 16$, the profiles clearly converge when viewed graphically. To quantify the convergence, measures similar to those introduced in Chapter 3 are used. An analytical solution is not available for this case, so each value is compared to the value obtained on the grid with the highest resolution of $512 \times 128 \times 256$ instead. Convergence of the geometrical representation, as measured by the length of lines from bottom to top of the vessel at different x can be seen in Figure 4.4. For

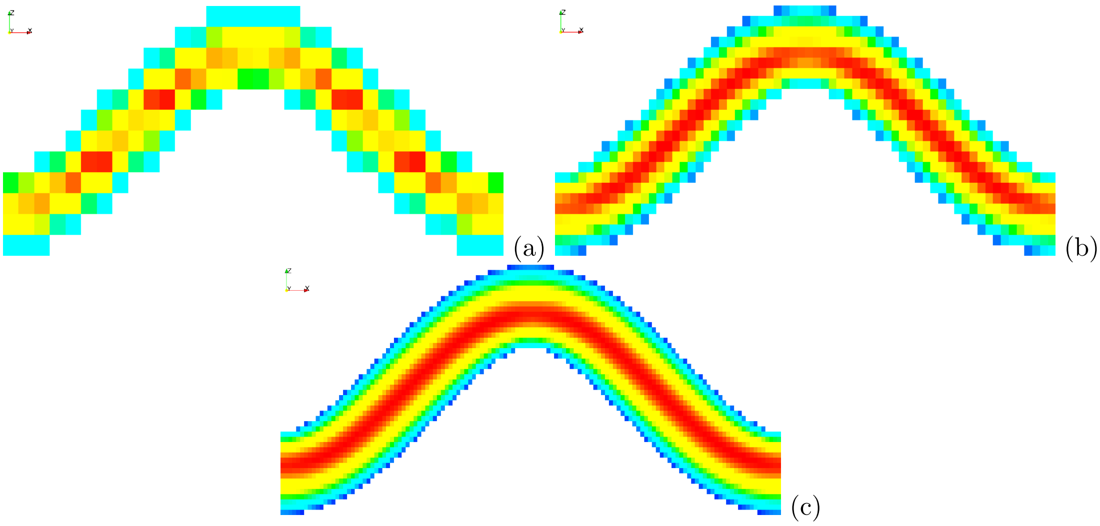

Figure 4.1: Slices of the velocity field through the center of a curved vessel with $\epsilon = 1$. Resolutions are (a) $32 \times 8 \times 16$ (b) $64 \times 16 \times 32$ (c) $128 \times 32 \times 64$. Colors correspond to the magnitude of the velocity vector, where blue corresponds to zero and red corresponds to the maximum velocity.

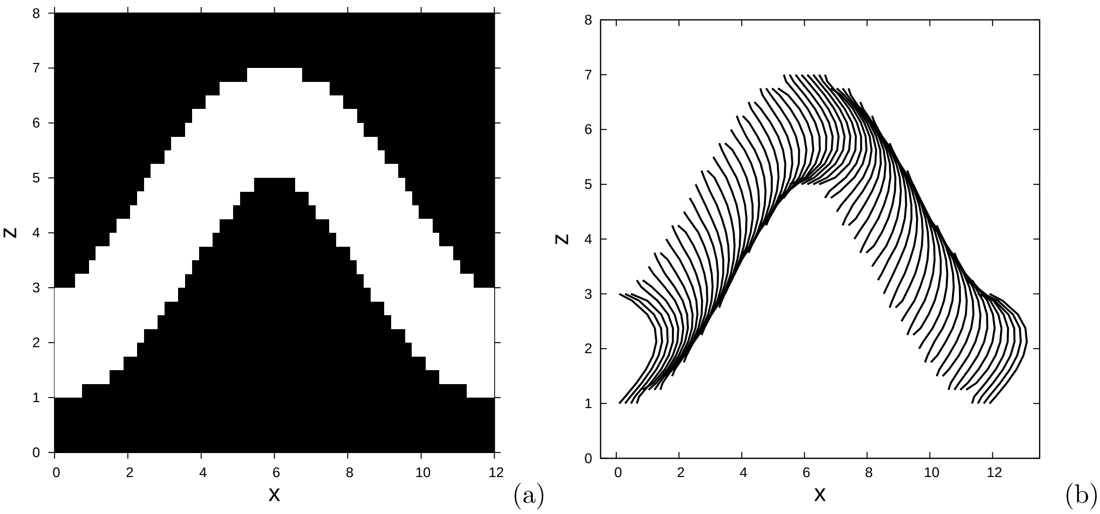

Figure 4.2: (a) Masking function on a plane through the center of a curved vessel with $\epsilon = 1$. (b) Velocity profiles on this plane at resolution $64 \times 16 \times 32$.

two locations this length does not change as the resolution is increased from $32 \times 8 \times 16$, since at these locations the outermost edges of the geometry coincide with grid points at the coarsest grid. At the other locations the length converges slightly faster than first order.

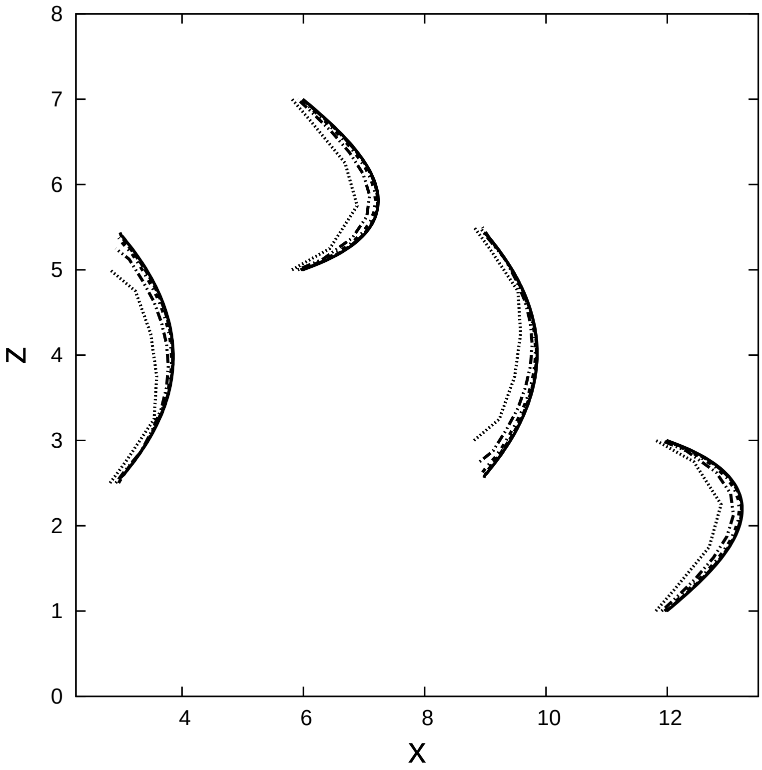

Figure 4.3: Velocity profiles on a plane through the center of a curved vessel with $\epsilon = 1$. Resolutions are ranging from $32 \times 8 \times 16$ to $512 \times 128 \times 256$, where the number of grid cells is doubled in every direction with each refinement, indicated by dots, dash-dot-dot, dash-dot, dashed and solid lines respectively.

Figure 4.5 shows the error of the integral of the streamwise velocity over lines from bottom to top of the vessel with respect to the value of the integral for a solution found on a grid with resolution $512 \times 128 \times 256$. The error clearly shows second order convergence and at some locations even higher order convergence is achieved.

The maximum streamwise velocity along lines from bottom to top of the vessel converges with second or even higher order, as can be seen in Figure 4.6. At two locations this maximum value gets very close to the maximum value found on a grid with resolution $512 \times 128 \times 256$.

Integrals over the entire volume of the vessel are also considered. In Figure 4.7 the error with respect to the value at resolution $512 \times 128 \times 256$ of the volume of the vessel, the volume integral of the streamwise velocity and the volume integral over the kinetic energy E can be seen. These three quantities show convergence which is close to second order.

By chosing $\epsilon = 0.5$ the vessel becomes slightly skewed. This skewness presents a problem. Although the centerline of the vessel is nicely periodic, the currently generated boundary is not. Extension of the geometry with a mirrored geometry solves this problem and a new geometry which is periodic in the x-direction is obtained. Slices of the velocity field are presented in

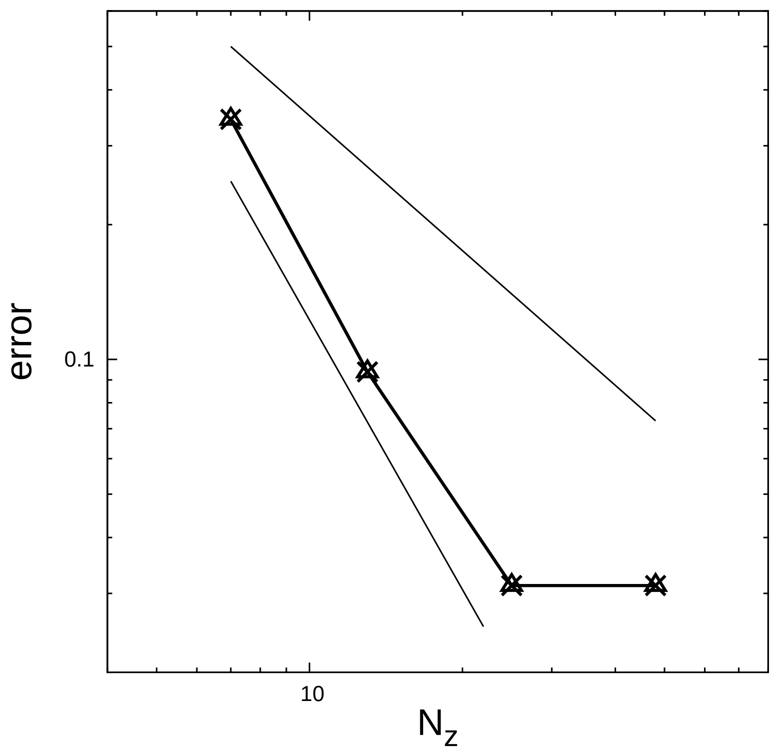

Figure 4.4: Error with respect to the numerical solution of the flow through the curved vessel with $\epsilon = 1$ at resolution $512 \times 128 \times 256$ of the length of the line from bottom to top in the z-direction at different streamwise locations $x_k = (\frac{kN_x}{4} - \frac{1}{2})\frac{L_x}{N_x}$, $k = 1 \dots 4$, where $L_x = 12$. The straight lines without markers have slope -1 and -2 respectively. For $k = 1, 3$ (crosses and triangles respectively) it converges with second order to a certain value.

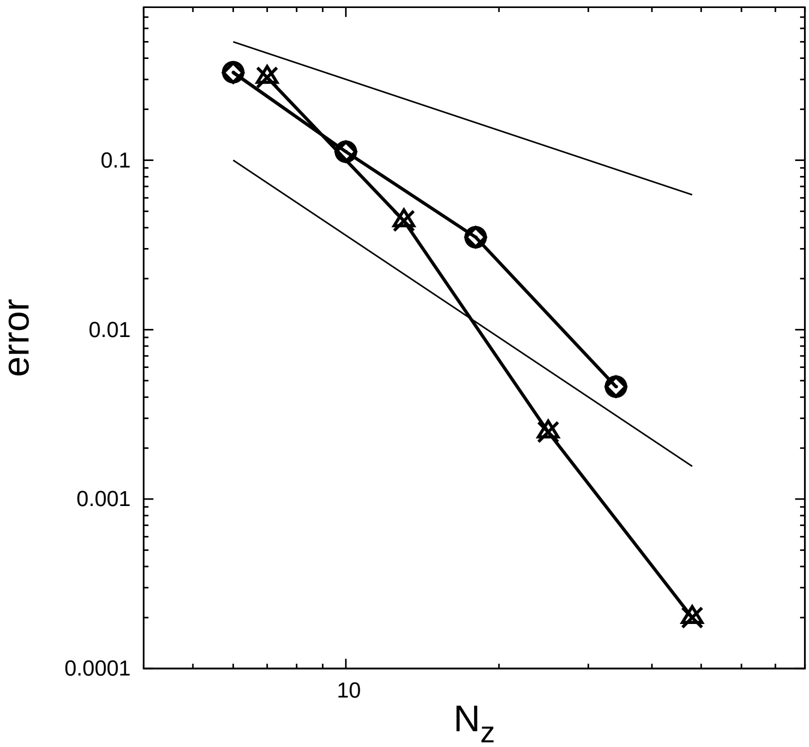

Figure 4.5: Error with respect to the numerical solution of the flow through the curved vessel with $\epsilon = 1$ at resolution $512 \times 128 \times 256$ of the streamwise velocity u integrated over the line from bottom to top in the z-direction at different streamwise locations $x_k = (\frac{kN_x}{4} - \frac{1}{2})\frac{L_x}{N_x}$, $k = 1 \ldots 4$, marked with crosses, circles, triangles and diamonds respectively, where $L_x = 12$. The straight lines without markers have slope -1 and -2 respectively.

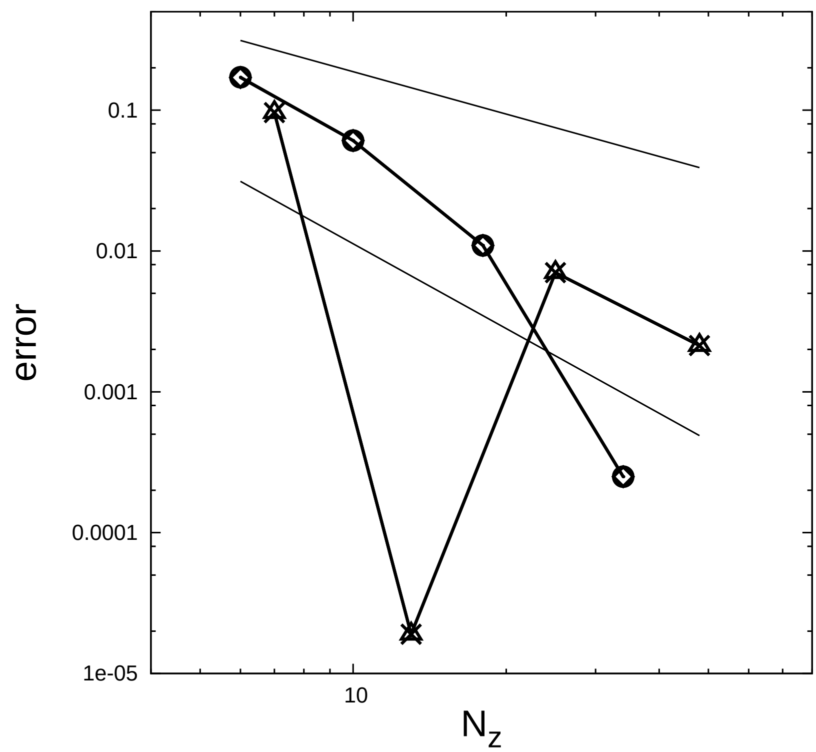

Figure 4.6: Error with respect to the numerical solution of the flow through the curved vessel with $\epsilon = 1$ at resolution $512 \times 128 \times 256$ of the maximum value of the streamwise velocity along the line from bottom to top at different streamwise locations $x_k = (\frac{kN_x}{4} - \frac{1}{2})\frac{L_x}{N_x}$, $k = 1 \ldots 4$, marked with crosses, circles, triangles and diamonds respectively, where $L_x = 12$. The straight lines without markers have slope -1 and -2 respectively.

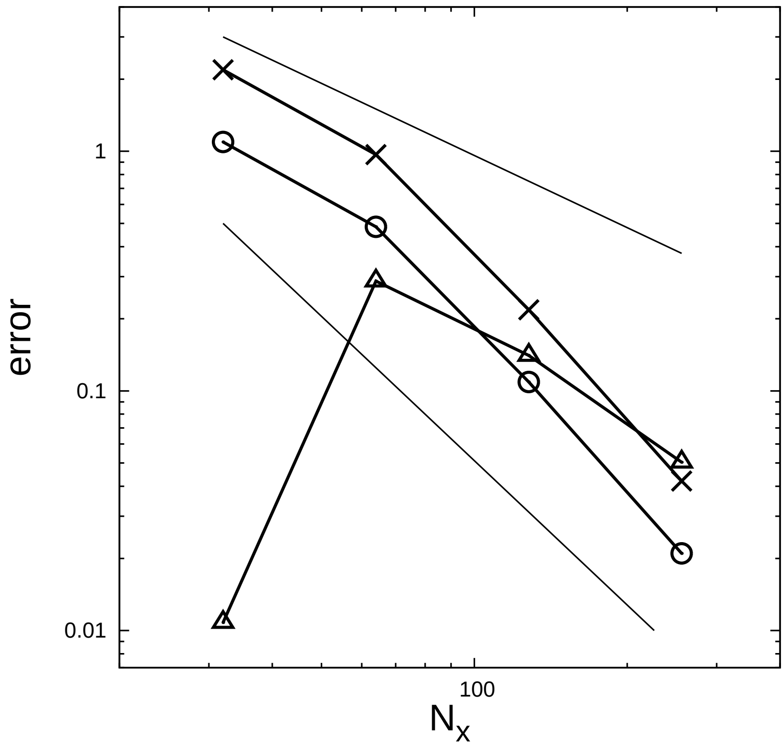

Figure 4.7: Error with respect to the numerical solution of the flow through the curved vessel with $\epsilon = 1$ at resolution $512 \times 128 \times 256$ of the integral $\int_V 1\,dV$ (crosses), the integral $\int_V u\,dV$ (circles) and the integral $\int_V E\,dV$ (triangles), where $E = \frac{1}{2}(u^2 + v^2 + w^2)$. The straight lines without markers have slope -1 and -2 respectively.

Figure 4.8, which clearly shows how the new geometry is formed from the original geometry and a mirrored geometry. Similar to the case with $\epsilon = 1$, the solution is poor at a coarse grid, but after refining the grid once good agreement can be seen with the solution which is found when the grid is refined even further.

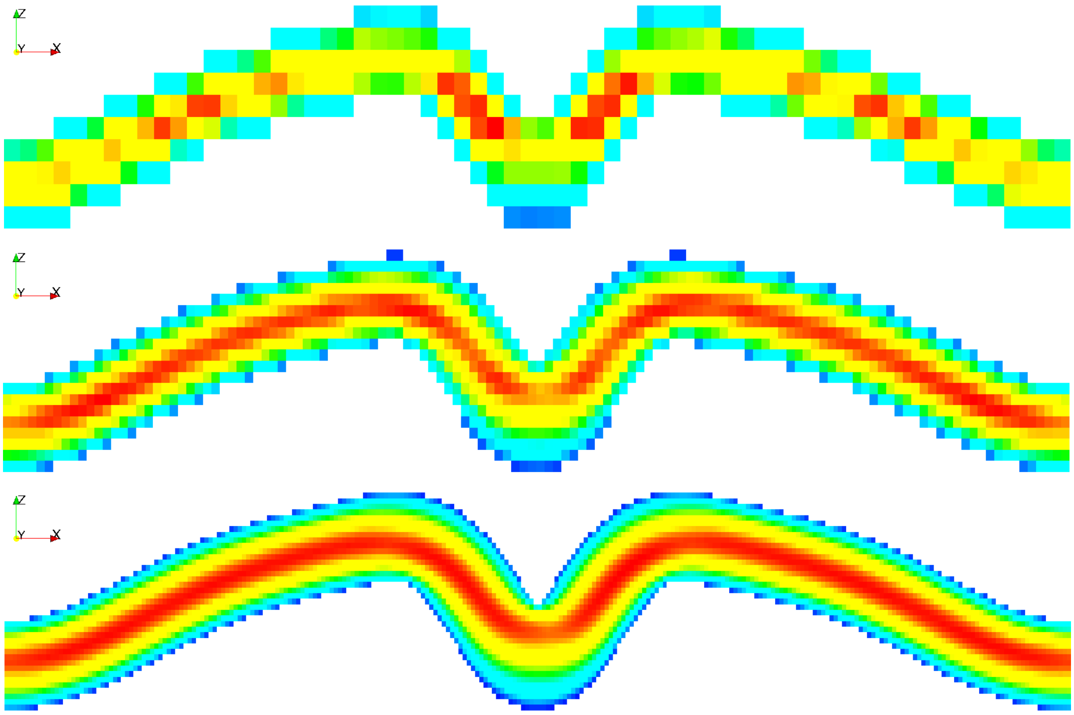

Figure 4.8: Slices of the velocity field through the center of a curved vessel with $\epsilon = 0.5$. Resolutions are (a) $32 \times 8 \times 16$ (b) $64 \times 16 \times 32$ (c) $128 \times 32 \times 64$. Colors correspond to the magnitude of the velocity vector, where blue corresponds to zero and red corresponds to the maximum velocity.

Figure 4.9 shows the masking function and profiles of the streamwise velocity at several streamwise locations on a plane through the center of the vessel. These profiles look similar to the profiles which were found for the case with $\epsilon = 1$.

In Figure 4.10 profiles of the streamwise velocity for different resolutions, ranging from $32 \times 8 \times 16$ to $512 \times 128 \times 256$, at several equidistant streamwise locations are shown. At each location the profiles appear to converge.

Figure 4.11 shows the error of the integral of the streamwise velocity over the lines from bottom to top of the vessel with respect to the value of the integral at resolution $512 \times 128 \times 256$. This integral clearly converges with second order, where convergence seems to be somewhat faster at locations where the profiles are more symmetrical.

The maximum value of the streamwise velocity along the lines from bottom to top of the vessel seems to behave in a similar way. As can be seen in Figure 4.12 these values also converge with second order with respect to the value at resolution $512 \times 128 \times 256$.

Figure 4.13 shows that for the integrals over the entire volume of the vessel the order of convergence is second order for the volume integrals indicated with crosses and circles and first order for the volume integral indicated with triangles. Similar orders of convergence were already

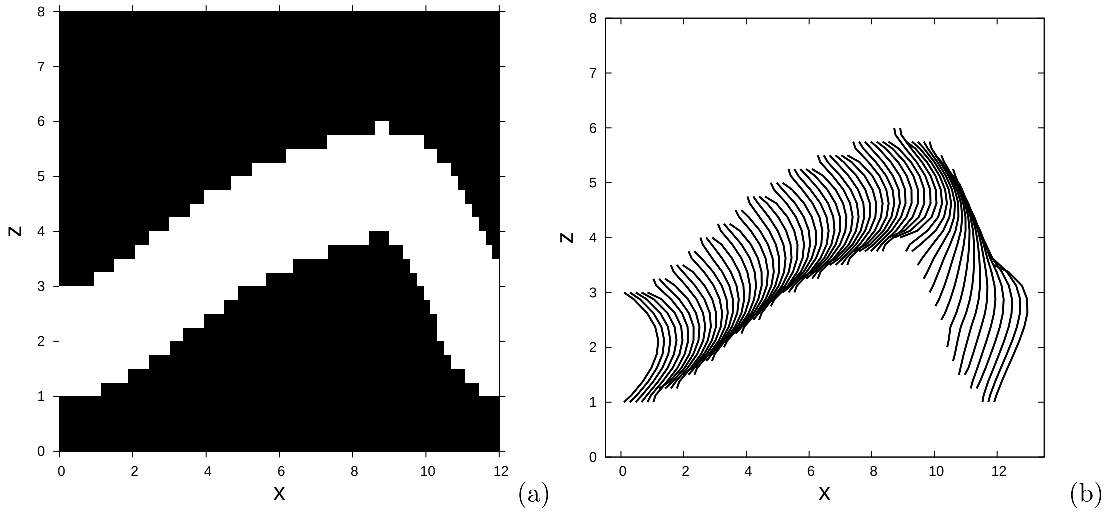

Figure 4.9: Velocity profiles on a plane through the center of a curved vessel with $\epsilon = 0.5$. The resolution shown here is $64 \times 16 \times 32$.

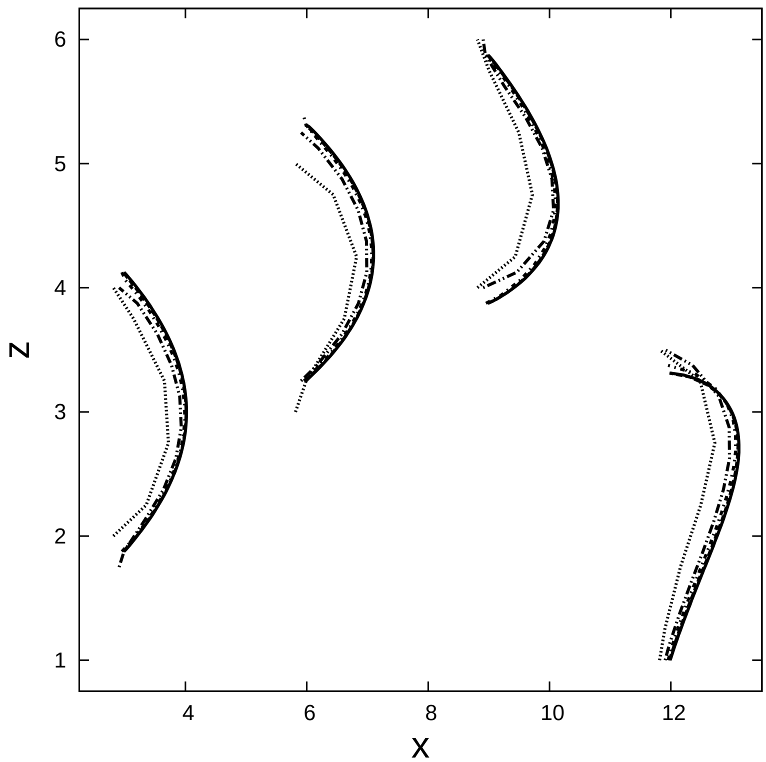

Figure 4.10: Velocity profiles on a plane through the center of a curved vessel with $\epsilon = 0.5$. Resulotions are ranging from $32 \times 8 \times 16$ to $512 \times 128 \times 256$, where the number of grid cells are doubled in every direction for each refinement, indicated with dots, dash-dot-dot, dash-dot, dashed and solid lines respectively.

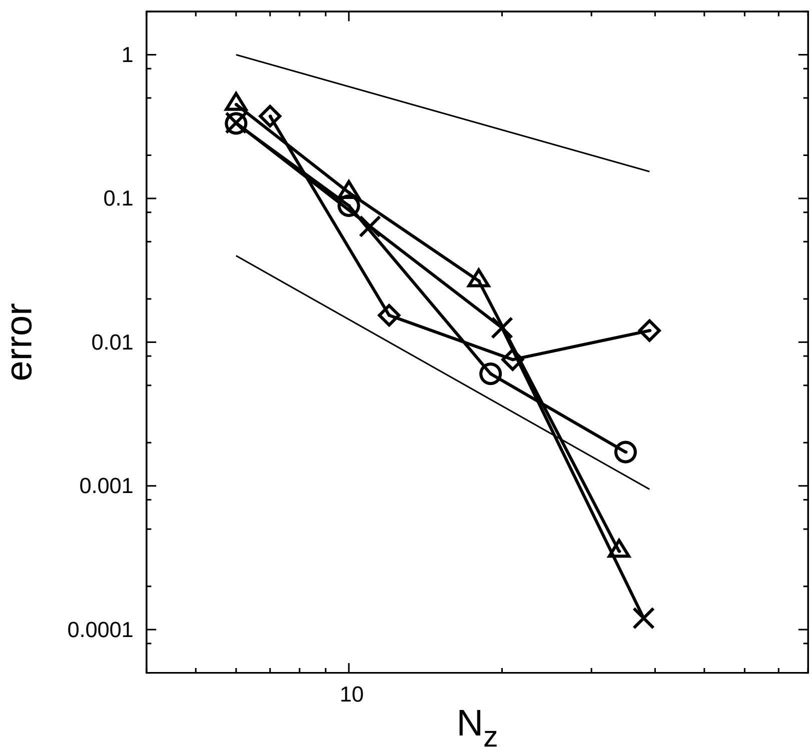

Figure 4.11: Error with respect to the numerical solution of the flow through the curved pipe with $\epsilon = 0.5$ at resolution $512 \times 128 \times 256$ of the integral $\int_{I_N(x_k)} u\, dz$ for $x_k = (\frac{kN_x}{4} - \frac{1}{2})\frac{L_x}{N_x}$, $k = 1 \ldots 4$, marked with crosses, circles, triangles and diamonds respectively, where $L_x = 12$. The straight lines without markers have slope -1 and -2 respectively.

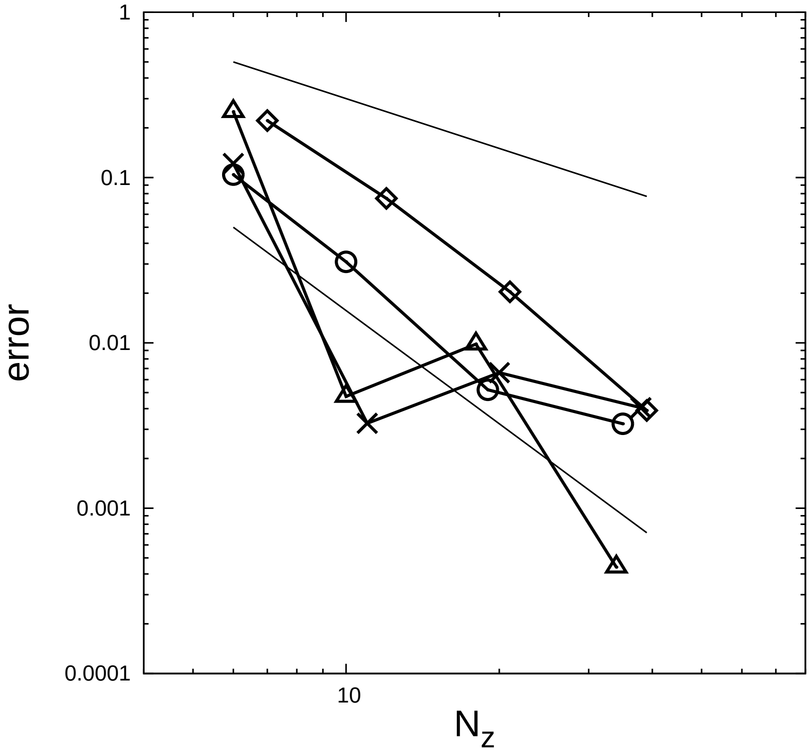

Figure 4.12: Error with respect to the numerical solution of the flow through the curved pipe with $\epsilon = 0.5$ at resolution $512 \times 128 \times 256$ of the maximum value of the streamwise velocity along the line from bottom to top of the vessel for different streamwise locations $x_k = (\frac{kN_x}{4} - \frac{1}{2})\frac{L_x}{N_x}$, $k = 1 \ldots 4$, marked with crosses, circles, triangles and diamonds respectively, where $L_x = 12$. The straight lines without markers have slope -1 and -2 respectively.

observed for the case with $\epsilon = 1$.

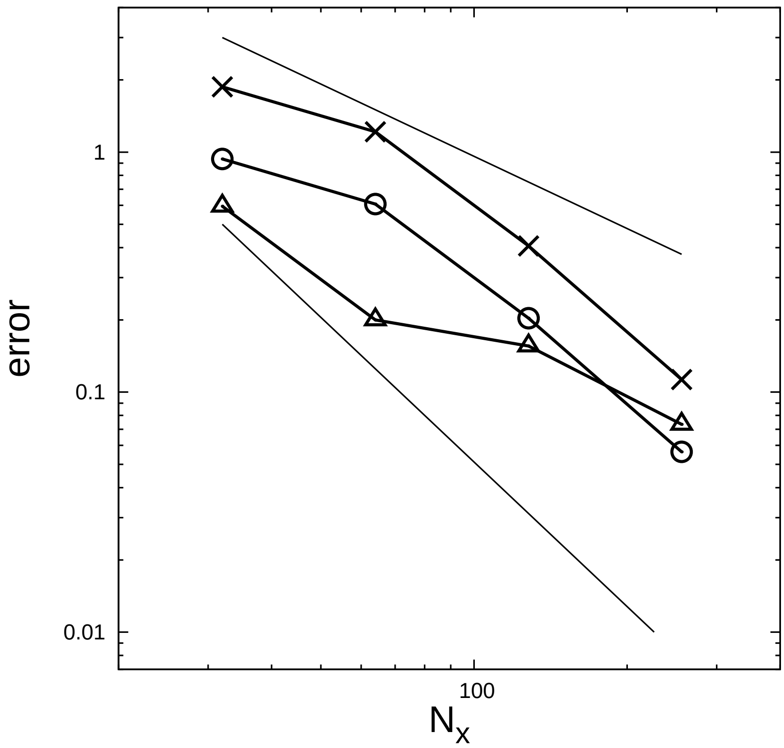

Figure 4.13: Error with respect to the numerical solution of the flow through the curved pipe with $\epsilon = 0.5$ at resolution $512 \times 128 \times 256$ of the integral $\int_V 1\, dV$ (crosses), the integral $\int_V u\, dV$ (circles) and the integral $\int_V E\, dV$ (triangles), where $E = \frac{1}{2}(u^2 + v^2 + w^2)$. The straight lines without markers have slope -1 and -2 respectively.

With $\epsilon = 0.25$ the vessel becomes even more skewed. Also with this case a mirrored geometry is used as extension to the original geometry to obtain periodicity in the x-direction. Figure 4.14 shows slices of the velocity field through the center of the vessel. Typical behavior is observed, where starting from a coarse grid with resolution $32 \times 8 \times 16$ the solution obtained after one refinement shows qualitative agreement with the solution at even finer grids.

In Figure 4.15 the masking function and profiles of the streamwise velocity on a plane through the centre of the vessel are shown. The increased skewness creates a fairly sharp transition in the geometry, as can be seen from the masking function, but this does not seem to affect the solution in a dramatic way at the selected flow conditions.

Profiles of the streamwise velocity at equidistant streamwise locations are shown in Figure 4.16. The profiles clearly converge. Even at locations where the geometry changes rapidly, convergence seems to be fairly good.

Convergence of the integral of the streamwise velocity over the line from top to bottom for several streamwise locations is clearly second order, as can be seen in Figure 4.17. The rate of convergence of the error with respect to the value of the integral at resolution $512 \times 128 \times 256$ seems to depend less on the location than for the previous two cases.

Again, the error of the maximum streamwise velocity with respect to the value at resolution

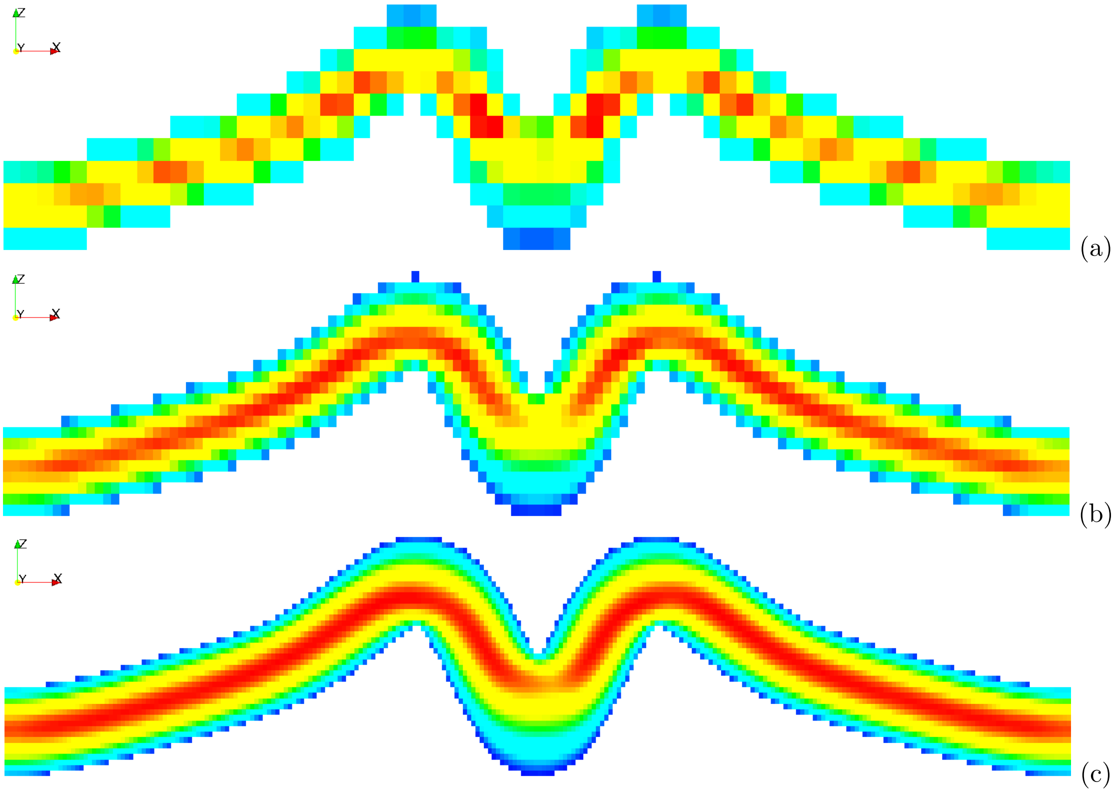

Figure 4.14: Slices of the velocity field through the center of a curved vessel with $\epsilon = 0.25$ with $\epsilon = 0.25$. Resolutions are (a) $32 \times 8 \times 16$ (b) $64 \times 16 \times 32$ (c) $128 \times 32 \times 64$. Colors correspond to the magnitude of the velocity vector, where blue corresponds to zero and red corresponds to the maximum velocity.

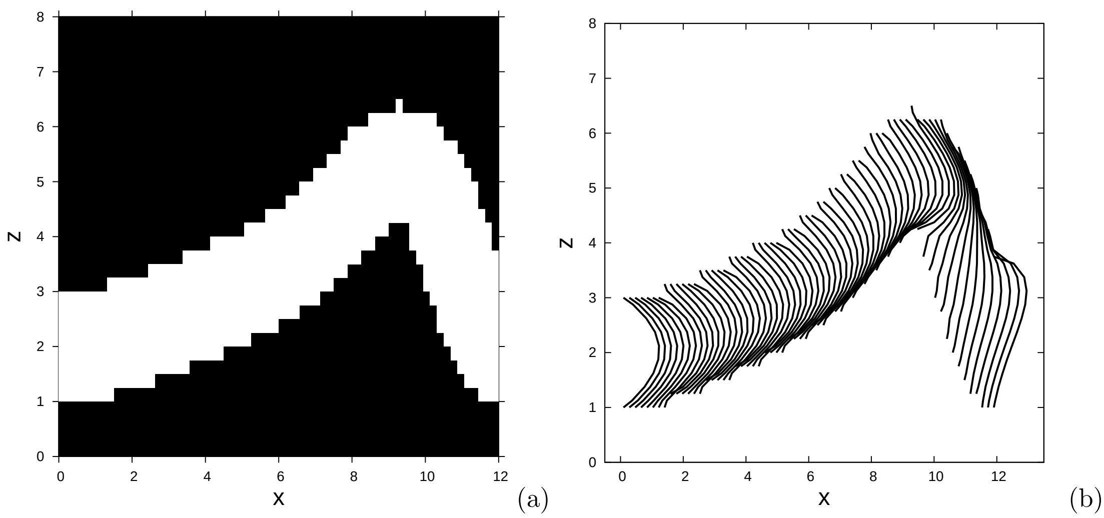

Figure 4.15: Velocity profiles on a plane through the centre of a curved vessel with $\epsilon = 0.25$. The resolution is $64 \times 16 \times 32$.

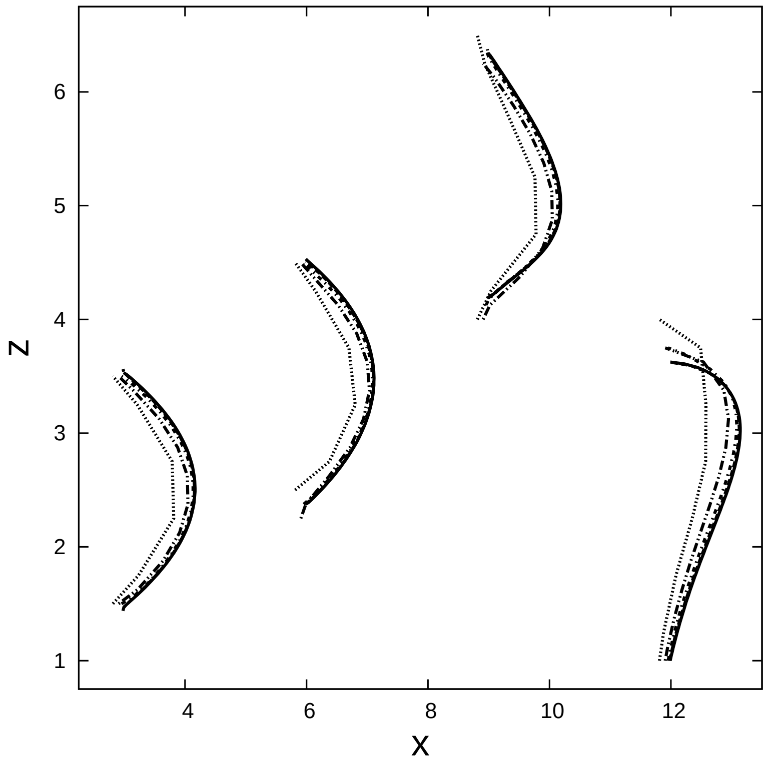

Figure 4.16: Velocity profiles on a plane through the center of a curved pipe with $\epsilon = 0.25$. Resolutions are ranging from $32 \times 8 \times 16$ to $512 \times 128 \times 256$, where the number of grid cells are doubled in every direction for each refinement.

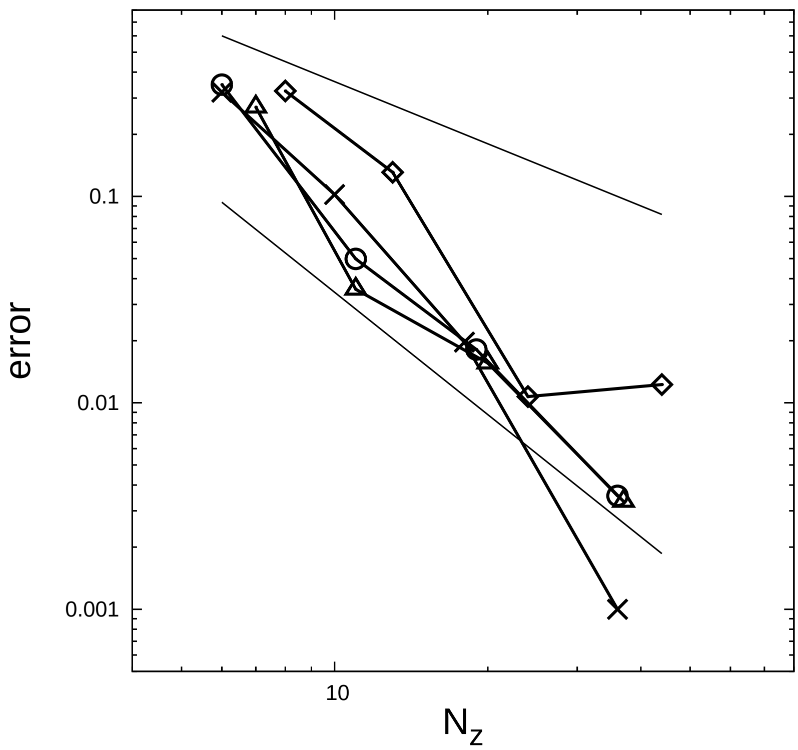

Figure 4.17: Error with respect to the numerical solution of the flow through the curved pipe with $\epsilon = 0.25$ at resolution $512 \times 128 \times 256$ of the integral $\int_{I_N(x_k)} u\, dz$ for $x_k = (\frac{kN_x}{4} - \frac{1}{2})\frac{L_x}{N_x}$, $k = 1 \ldots 4$, marked with crosses, circles, triangles and diamonds respectively, where $L_x = 12$. All lines seem to indicate second order convergence. The straight lines without markers have slope -1 and -2 respectively.

$512 \times 128 \times 256$ seems to give the same conclusion as the error of the integral of the streamwise velocity. As can be seen in Figure 4.18, the maximum streamwise velocity converges with second order, and at one location even with higher order.

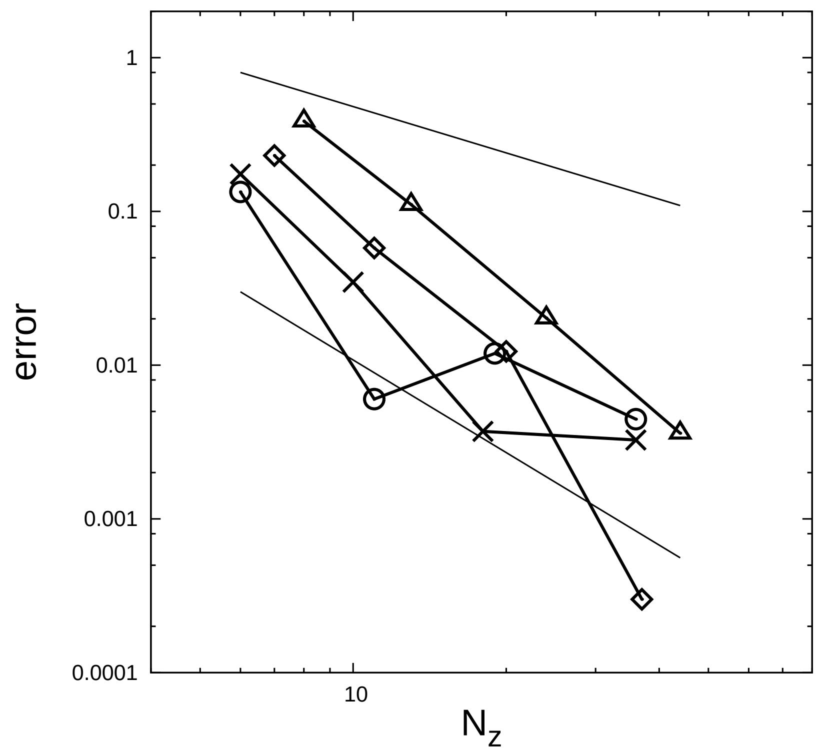

Figure 4.18: Error with respect to the numerical solution of the flow through the curved pipe with $\epsilon = 0.25$ at resolution $512 \times 128 \times 256$ of the maximum value of the streamwise velocity along a line from bottom to top for streamwise locations $x_k = (\frac{kN_x}{4} - \frac{1}{2})\frac{L_x}{N_x}$, $k = 1 \ldots 4$, marked with crosses, circles, triangles and diamonds respectively, where $L_x = 12$. The straight lines without markers have slope -1 and -2 respectively.

The errors of the integrals over the entire volume of the vessel with respect to the value at resolution $512 \times 128 \times 256$, which are presented in Figure 4.19, very clearly show second order convergence.

With these three cases it was shown that it is possible to simulate laminar flow in curved vessels, even if they are skewed. Results in terms of profiles and convergence of different quantities are convincing enough to assume that it is possible to simulate laminar flow in realistic geometries as well.

4.2 Realistic geometry and flow conditions

In this section flow through a realistic geometry is considered. This geometry is constructed from a masking function, which was obtained after manipulation of a 3DRA scan. Both laminar flow and flow at a realistic Reynolds number are considered. After a qualitative inspection of the flow

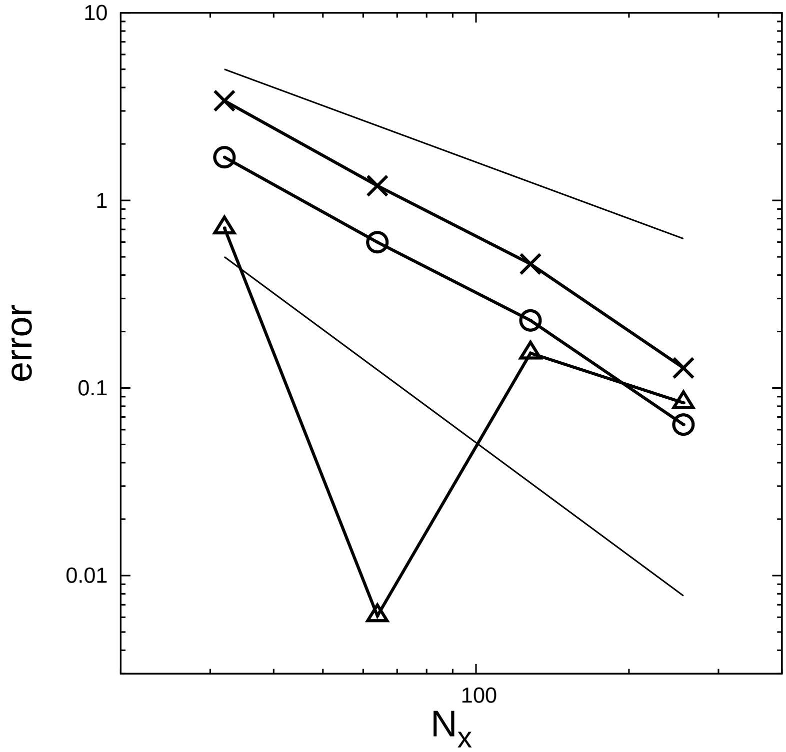

Figure 4.19: Error with respect to the numerical solution of the flow through the curved pipe with $\epsilon = 0.25$ at resolution $512 \times 128 \times 256$ of the integral $\int_V 1\,dV$ (solid), the integral $\int_V u\,dV$ (dashed) and the integral $\int_V E\,dV$ (dotted), where $E = \frac{1}{2}(u^2 + v^2 + w^2)$. The bold lines have slope -1 and -2 respectively.

by looking at streamlines and contour plots of the streamwise velocity, a convergence study is done for the laminar flow. It will become clear that convergence is much harder to achieve for the realistic flow.

The vessel under consideration has radius $R = 1.94 \cdot 10^{-3}$(m), a typical value for a vessel in the circle of Willis, the mayor system supplying blood to the brain. The kinematic viscosity of blood is $\nu = 3.01 \cdot 10^{-6}$ (m^2/s). Figure 4.20 shows streamlines of laminar flow with average streamwise velocity $\bar{u} = 1.55 \cdot 10^{-3}$ (m/s) through the vessel, corresponding to a Reynolds number Re = 1. The streamlines indicate that the main flow does not enter the cavity of the aneurysm at the selected flow condition.

Figure 4.20: Streamlines of laminar flow through a geometry constructed from a masking function, which was obtained after manipulation of a 3DRA scan, at resolution $256 \times 128 \times 256$.

In Figure 4.21 the streamlines of realistic flow with average streamwise velocity $\bar{u} = 0.388$ (m/s) is shown, corresponding to Re = 250. The behavior of the flow changes drastically, compared to Re = 1. Streamlines now do enter the cavity of the aneurysm and the flow appears to become somewhat unsteady, even in parts of the domain where the geometry changes smoothly.

Contour lines of the streamwise velocity of laminar flow at two different locations, one being in the part of the domain where the geometry changes smoothly and one near the opening of the cavity of the aneurysm, are shown in Figure 4.22. Both in Figure 4.22(a) and the lower part of Figure 4.22(b) a flow reminiscent of Poiseuille flow can be recognised. Figure 4.22(b) also confirms that the main flow does not enter the cavity of the aneurysm. The solutions seems to converge relatively fast, the contour lines at resolution $128 \times 64 \times 128$ look a lot like the contour lines at resolution $256 \times 128 \times 256$.

Figure 4.23 shows contour lines of the streamwise velocity of realistic flow at the previously mentioned locations at different times. Although the unsteady character of the flow is clearly visible, similar structures arise at different times. Figure 4.23(a) shows that flow is mainly in the

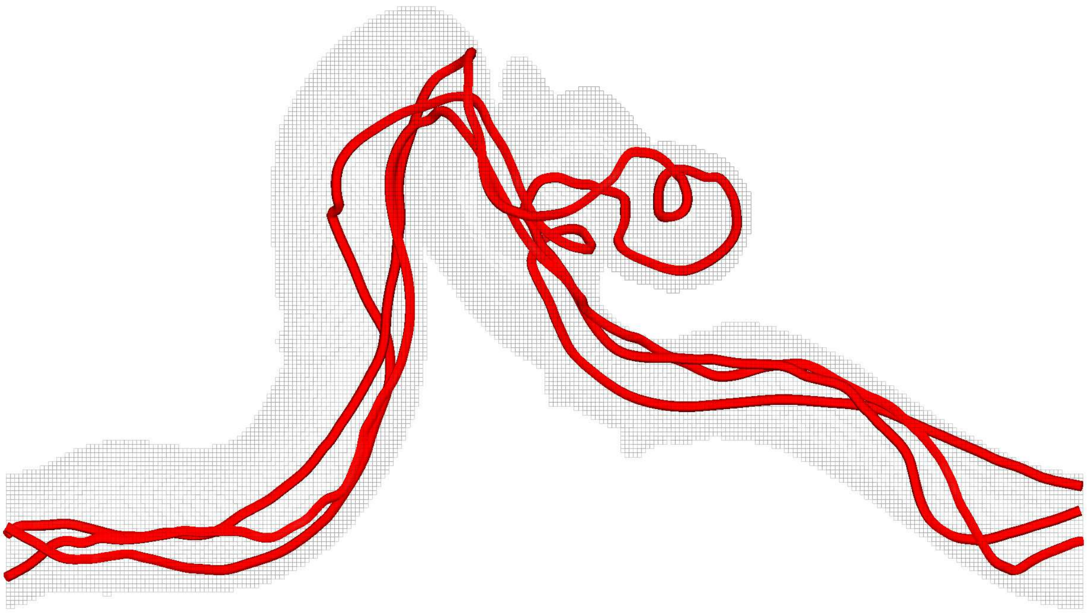

Figure 4.21: Streamlines of flow at Re = 250 through a geometry constructed from a masking function, which was obtained after manipulation of a 3DRA scan, at resolution $256 \times 128 \times 256$.

streamwise direction and small areas of backflow appear at the top of the vessel. In Figure 4.23-(b) a large area of backflow can be recognised at the top of the vessel, while areas of flow in the streamwise direction are mainly at the bottom and at the right side of the vessel.

In Figure 4.24 profiles of the streamwise velocity of laminar flow through the vessel are shown. The convergence of the solution, which dominates especially in the smooth part of the domain, can be very clearly seen in this figure.

When looking at profiles of the streamwise velocity in the developing phase of realistic flow through the vessel, as can be seen in Figure 4.25, it is clear that the solution indeed converges rather poorly. However, certain features of the flow can be recognised over different resolutions. The locations of extreme values are approximately the same for different resolutions.

The convergence of the profiles of the streamwise velocity that was observed for laminar flow also becomes apparent in Figure 4.26, which shows that the integral over the streamwise velocity and the maximum streamwise velocity converge with second or higher order.

The volume of the vessel and the integrals of the streamwise velocity and kinetic energy over the volume of the vessel very clearly converge with second order, as can be seen in Figure 4.27.

Although the profiles of the streamwise velocity of realistic flow showed very little convergence, the integral of the streamwise velocity over a line in the smooth part of the domain still converges with second order, as can be seen in Figure 4.28. The integral of the streamwise velocity over a line near the opening of the cavity of the aneurysm and the maximum streamwise velocity along these lines converge with an order which is much closer to first order.

Figure 4.29 shows that the integral of the streamwise velocity over the volume of the vessel converges with second order, as was the case for laminar flow. It also shows that the integral of the kinetic energy over the volume of the vessel converges with an order which is at least higher than first order.

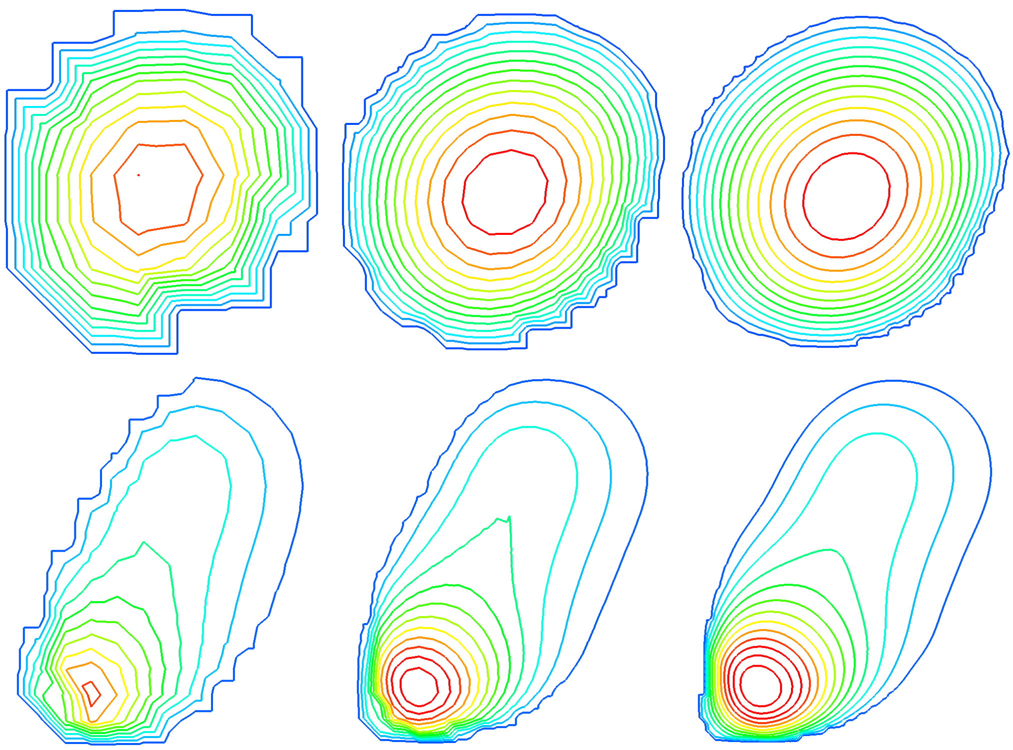

(a)

(b)

Figure 4.22: Contour lines of the streamwise velocity of laminar flow on cross sections in the $y-z$ plane at 1/16th (a) and half (b) of the domain in the x-direction. The values of the contour lines in (a) are uniformly distributed on the interval $[0, 6.30 \cdot 10^{-3}]$ and in (b) on the interval $[-7.53 \cdot 10^{-6}, 4.58 \cdot 10^{-3}]$. From left to right the resolutions are $64 \times 32 \times 64$, $128 \times 64 \times 128$ and $256 \times 128 \times 256$.

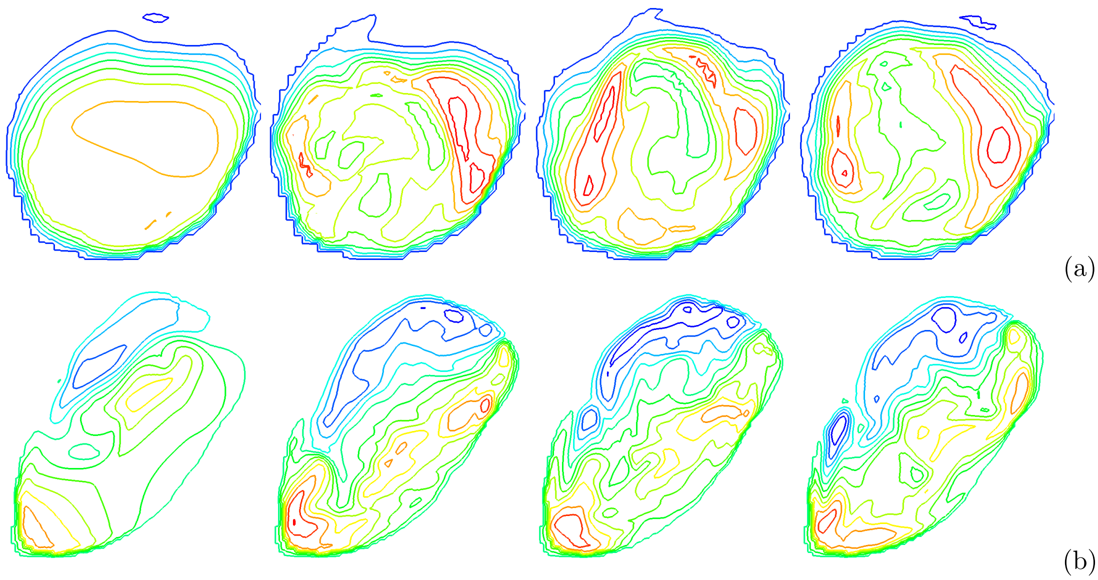

Figure 4.23: Contour lines of the streamwise velocity of realistic flow with Re = 250 on cross sections in the $y-z$ plane at 1/16th (a) and half (b) of the domain in the x-direction at resolution $256 \times 128 \times 256$. The values of the contour lines in (a) are uniformly distributed on the interval $[-0.292, 2.16]$ and in (b) on the interval $[-0.909, 1.42]$. From left to right time increases from 0.01 to 0.4 with increment $\Delta t = 0.13$.

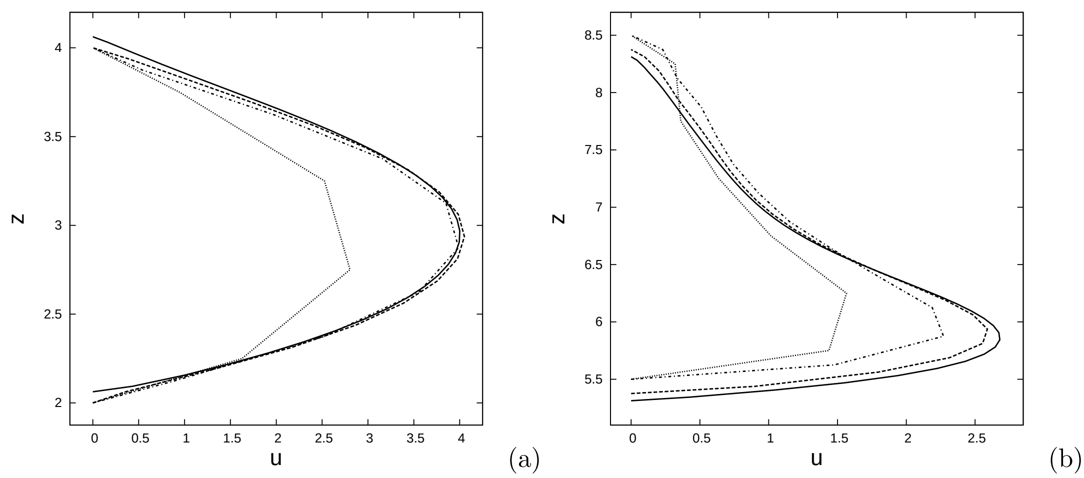

Figure 4.24: Profiles of the streamwise velocity in dimensionless quantities of laminar flow at 1/16th of the domain in the x-direction and 13/16th of the domain in the y-direction (a), and at half of the domain in both the x-direction and the y-direction (b). Resolutions are $32 \times 16 \times 32$ (dots), $64 \times 32 \times 64$ (dash-dot), $128 \times 64 \times 128$ (dash) and $256 \times 128 \times 256$ (solid).

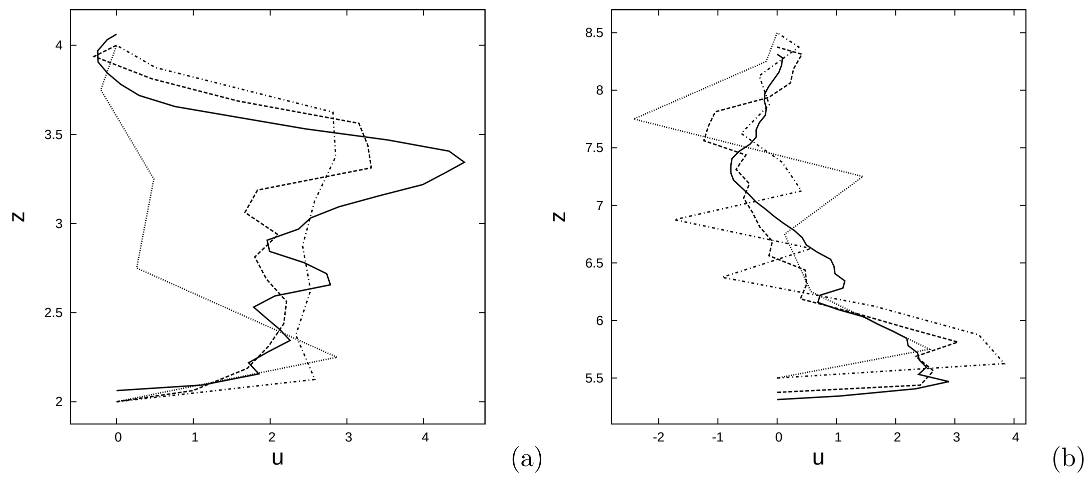

Figure 4.25: Profiles of the streamwise velocity in dimensionless quantities in the developing phase, at $t = 0.01$, of realistic flow with Re = 250 at 1/16th of the domain in the x-direction and 13/16th of the domain in the y-direction (a), and at half of the domain in both the x-direction and the y-direction (b). Resolutions are $32 \times 16 \times 32$ (dots), $64 \times 32 \times 64$ (dash-dot), $128 \times 64 \times 128$ (dash) and $256 \times 128 \times 256$ (solid).

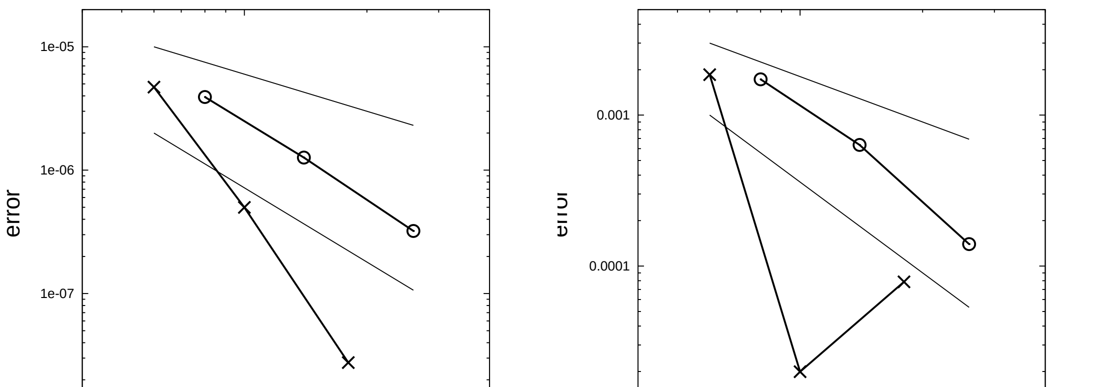

Figure 4.26: Error with respect to the numerical solution of laminar flow through the vessel at resolution $256 \times 128 \times 256$ on lines from bottom to top of the vessel at 1/16th of the domain in the x-direction and 13/16th of the domain in the y-direction (crosses), and at half of the domain in both the x-direction and the y-direction (circles). In (a) the error of the integral of the streamwise velocity over the lines is shown and (b) shows the error of the maximum streamwise velocity along the lines. The straight lines without markers have slope -1 and -2 respectively.

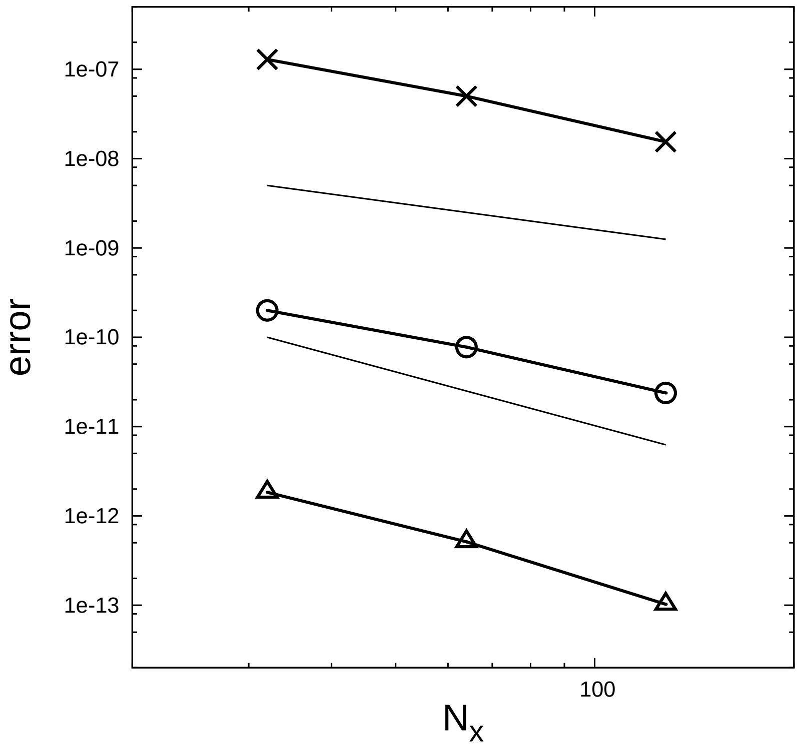

Figure 4.27: Error with respect to the numerical solution of laminar flow through the vessel at resolution $256 \times 128 \times 256$ of the integral $\int_V 1\,dV$ (crosses), the integral $\int_V u\,dV$ (circles) and the integral $\int_V E\,dV$ (triangles), where $E = \frac{1}{2}(u^2 + v^2 + w^2)$. The straight lines without markers have slope -1 and -2 respectively.

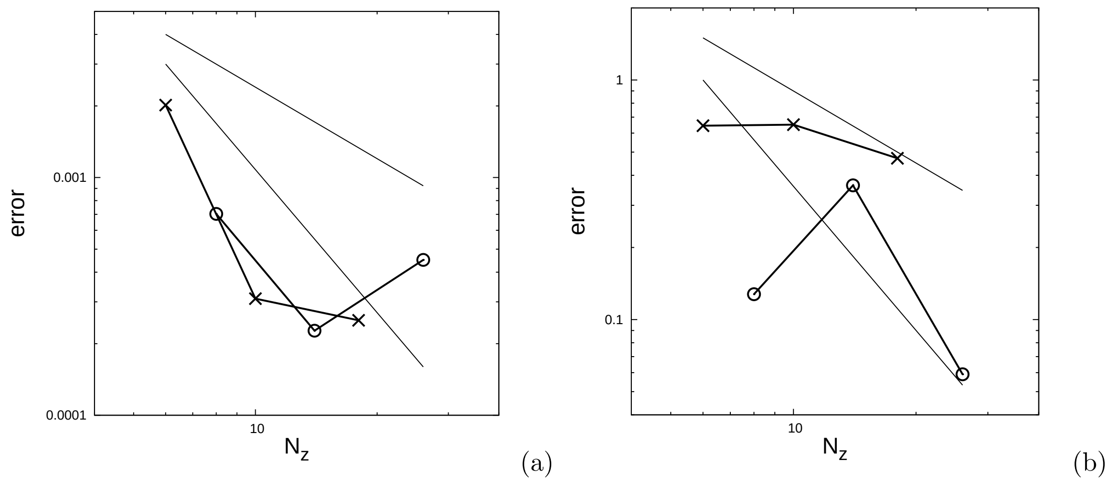

Figure 4.28: Error with respect to the numerical solution of realistic flow at Re = 250 through the vessel at resolution 256 × 128 × 256 on lines from bottom to top of the vessel at 1/16th of the domain in the x-direction and 13/16th of the domain in the y-direction (crosses), and at half of the domain in both the x-direction and the y-direction (circles). In (a) the error of the integral of the streamwise velocity over the lines is shown and (b) shows the error of the maximum streamwise velocity along the lines. The straight lines without markers have slope -1 and -2 respectively.

When comparing the average pressure drop over the vessel for laminar and realistic flow in Figure 4.30, a significant difference in temporal behavior can be seen. After a short period of highly oscillatory behavior associated with the transient following the unrealistic initial condition of zero flow, the global pressure gradient stabilises and remains constant for laminar flow, whereas the global pressure gradient for realistic flow continues with a lower amplitude oscillation.

The initial errors for each of the components of the fluid velocity in the iterative method to solve the momentum equations are shown in Figure 4.31. The termination criterion for the iterative method requires that this error is lower than 10^{-5}. Even after this criterion is met by the initial errors, the initial errors continue to decrease and have decreased with nine decades by the end of the simulation for laminar flow. In case of realistic flow at Re = 250 the criterion is never met by the initial errors. In fact, the initial errors decrease with four decades and then level out with a small amplitude oscillation. This corresponds with the observed unsteady flow behavior. The residuals never can become very small in such conditions.

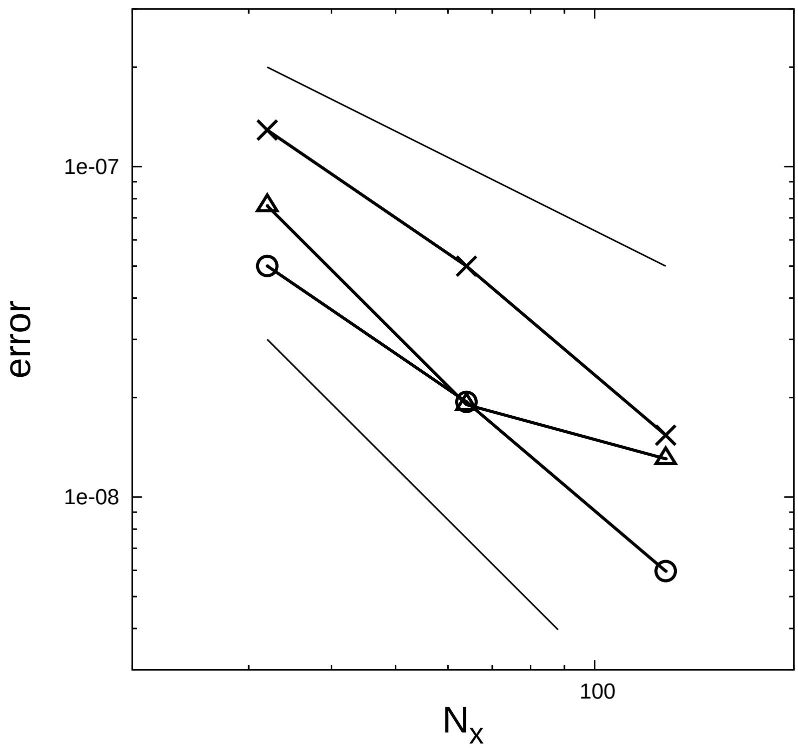

Figure 4.29: Error with respect to the numerical solution of realistic flow at Re = 250 through the vessel at resolution 256 × 128 × 256 of the integral $\int_V 1\,dV$ (crosses), the integral $\int_V u\,dV$ (circles) and the integral $\int_V E\,dV$ (triangles), where $E = \frac{1}{2}(u^2 + v^2 + w^2)$. The straight lines without markers have slope −1 and −2 respectively.

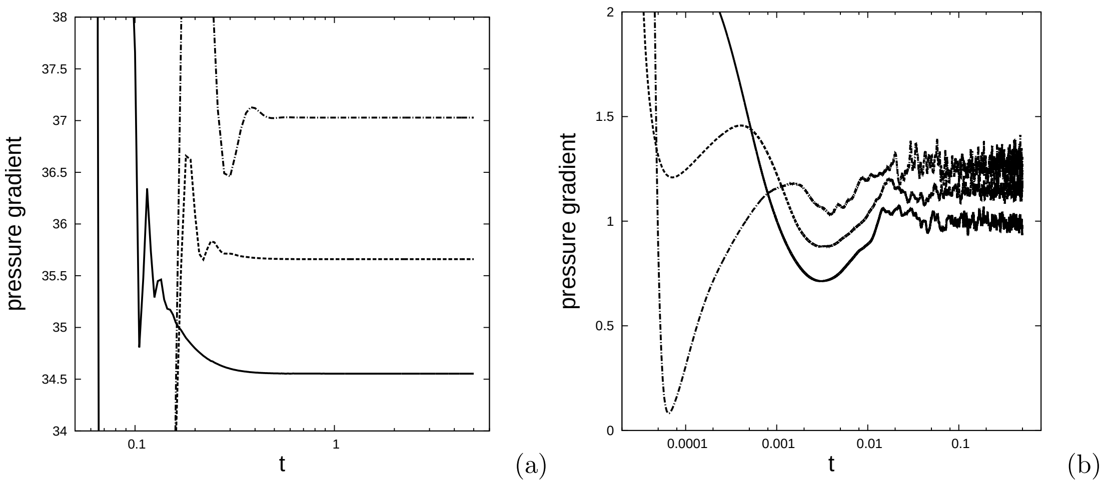

Figure 4.30: Evolution of the global pressure gradient in the streamwise direction, shown in dimensionless quantities, at different resolutions for both laminar flow (a) and realistic flow (b). Resolutions are 64 × 32 × 64 (dash-dot), 128 × 64 × 128 (dash) and 256 × 128 × 256 (solid).

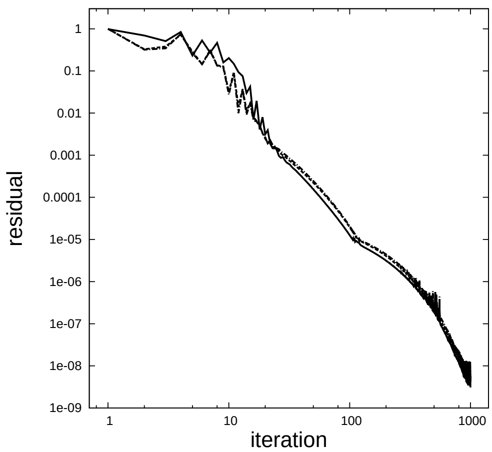

(a)

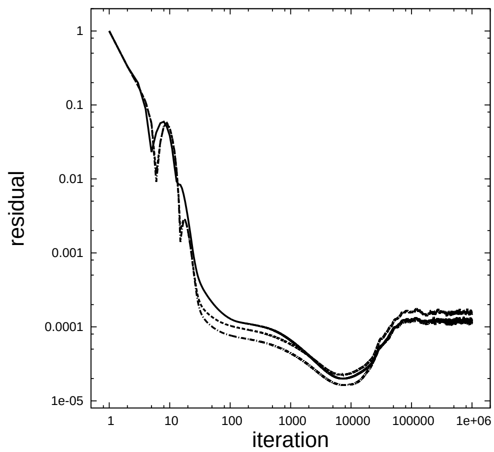

(b)

Figure 4.31: Initial errors in the iterative method to solve the momentum equations for each time step of the velocity in the x-direction (solid), y-direction (dashed), z-direction (dash-dot) for both laminar flow (a) and realistic flow (b) through the vessel.

Chapter 5

Discussion and outlook

The main goal of this project was to simulate blood flow in the human brain with OpenFOAM. The immersed boundary (IB) method has proven to be a suitable method for these type of simulations. With the IB method, a geometry is simply immersed in a Cartesian grid and is respresented by means of a masking function. This masking function is a binary function which equals zero if a grid cell is part of the geometry and one otherwise. While complex and time consuming grid generation is prevented, the simplicity of the IB method is in itself a disadvantage. Namely, often only a small portion of the grid cells are part of the geometry, which makes the IB method a rather inefficient method in terms of computation time. In this project an effort was made to construct a grid in OpenFOAM from the masking function, including only grid cells which are part of the geometry. To construct the grid, OpenFOAM requires a number of input files. The challenge was to extract the grid cells which are part of the geometry from the masking function in an efficient way and generate the input files accordingly. This was done succesfully and the most important requirements posed by OpenFOAM on the input files were presented in this thesis.

To validate the approach in this thesis, Poiseuille flow through a cylindrical pipe was considered. As expected, a first-order convergence of the numerical solution was observed. This corresponds to what was found by Mikhal [2]. When laminar flow through a curved pipe was also examined, the numerical solution showed an unexpected second-order convergence. In the study by Mikhal this superconvergence, which was attributed to the symmetry of the domain in this thesis, was not observed. Attempts to recover first-order convergence by increasing the skewness of the curved pipe, thus breaking symmetry, did not succeed. The superconvergence of the numerical solutions for curved pipes deserves further attention. Results from simulations of flow through these model geometries were convincing enough to assume that simulations of laminar flow through a realistic geometry, which was extracted from 3D rotational angiography (3DRA) data, would give reliable results as well. Indeed, the resulting numerical solutions behaved as expected and showed no abnormalities. Velocity profiles at different locations in the blood vessel even suggested a second-order convergence. Simulations at higher resolutions could confirm this. Naturally, the resolution of the grid is limited by the resolution of the original 3DRA data. Simulations of flow at physiological flow rates revealed unsteady behavior of the flow. This is a remarkable result, since Mikhal explicitly reports steady flow at these flow rates.

The current approach can be improved upon in several ways. The staircase approximation of the geometry led to first-order, and even second-order, convergence of the numerical solution. It would be an interesting topic of research to do a similar study with a smoothened geometry, e.g. by adding cells with a prism shape. A crucial part in further development of the currently available tools is automation. To smoothen the process from masking function to performing simulations in OpenFOAM, the fact that OpenFOAM allows its users to create their own applications could be utilised to build an application which generates the input files for the grid, if a masking function is supplied.

Bibliography

[1] R.I Issa. Solution of the implicitly discretised fluid flow equations by operator-splitting. *Journal of Computational Physics*, 62(1):40 – 65, 1986.

[2] Julia Mikhal. *Modeling and simulation of flow in cerebral aneurysms.* PhD thesis, University of Twente, Enschede, October 2012.

[3] OpenFOAM Foundation. *OpenFOAM Programmer's guide*, May 2012. Version 2.1.1.